Chemical Engineering Journal 422 (2021) 129627

Contents lists available at ScienceDirect

Chemical Engineering Journal

journal homepage: www.elsevier.com/locate/cej

Continuous enantioselective crystallization of chiral compounds in coupled fluidized beds

J. Gänsch [a], N. Huskova [a,b], K. Kerst [c,d], E. Temmel [a,e], H. Lorenz [a], M. Mangold [b], G. Janiga [c], A. Seidel-Morgenstern [a,f,*]

[a] Max Planck Institute for Dynamics of Complex Technical Systems, Sandtorstraße 1, 39106 Magdeburg, Germany
[b] Bingen University of Applied Sciences, Berlinstraße 109, 55411 Bingen am Rhein, Germany
[c] Laboratory of Fluid Dynamics and Technical Flows, Otto von Guericke University, Universitätsplatz 2, 39106 Magdeburg, Germany
[d] Institute of Urban and Industrial Water Management, TU Dresden, 01062 Dresden, Germany
[e] Sulzer Chemtech Ltd, Gewerbestrasse 28, 4123 Allschwil, Switzerland
[f] Institute of Process Engineering, Otto von Guericke University, Universitätsplatz 2, 39106 Magdeburg, Germany

ARTICLE INFO

Keywords:
Chiral separation
Continuous preferential crystallization
Fluidized beds
Population balance model
CFD-DEM simulation
Asparagine monohydrate

ABSTRACT

This review summarizes results of an interdisciplinary project devoted to improve the access to enantiopure components by applying an advanced continuous separation process exploiting the principle of kinetically controlled preferential crystallization within two coupled fluidized beds located in conically shaped tubular crystallizers. The process efficiently combines selective crystallization with integrated product classification. Along with summarizing the related literature, new original results are presented with respect to theoretical process description and experimental validation. Although only one chiral system is considered specifically, namely the separation of the enantiomers of a racemic mixture of asparagine monohydrate using water as solvent, general conclusions will be drawn to highlight the large potential of the process principle. The conceptual approaches presented are seen as useful tools for the development of productive continuously operating enantioselective crystallization processes. They are applicable to separate enantiomers of numerous chiral molecules.

1. Introduction: chirality and enantiomers

Enantiomers are pairs of optically active stereoisomers, which are non-superimposable mirror images of each other. They can exist as levorotatory (−) and dextrorotatory (+) molecules and are denominated as D and L or (*R*) and (S) [1]. For amino acids the classical D/L notation is widely used. In living organisms L-amino acids clearly predominate over the D-ones, a fact not fully fathomed up to now [2,3]. In the life science industries, manufacturing pharmaceuticals, food and agrochemicals there is a large interest to produce single enantiomers [4–7]. Regulators increasingly demand that chiral drugs are administered in optically pure form. This has intensified efforts of industrial and academic research devoted to develop techniques, which are capable to produce pure enantiomers.

The approaches applied to supply pure enantiomers of chiral molecules can be divided into two groups: A) the *chiral approach* based on developing an *asymmetric synthesis* of only the desired enantiomer and B) the *racemic approach* based on *separating mixtures* of both enantiomers [8].

In the last decades remarkable progress has been achieved in the field of asymmetric synthesis [9–11]. An overview regarding the status of separating enantiomers was given in 2014 [8]. In this broader oriented review was summarized the significant progress achieved in the last decades in applying chromatographic [12,13] and crystallization based techniques. Only the second *racemic approach* will be considered below.

In the next section crystallization-based resolution methods will be introduced focusing on exploiting the attractive concept of preferential crystallization, which possesses significant potential to be applied in efficient continuous enantioseparation processes.

2. Crystallization as a separation process

Crystallization is an important technology for separation, purification and formulation in the chemical industry. It is used for both large scale production, for example to provide inorganic salts for fertilizers

* Corresponding author.
E-mail address: seidel@mpi-magdeburg.mpg.de (A. Seidel-Morgenstern).

https://doi.org/10.1016/j.cej.2021.129627
Received 4 January 2021; Received in revised form 23 March 2021; Accepted 29 March 2021
Available online 10 April 2021

produced in million tons per year, and for the production of pharmaceuticals, which are often required only at a few kg scale [14–16]. The essential step is the transition of a single substance or of several substances from gaseous, liquid (or dissolved) or amorphous solid state to the crystalline state. It is particularly important as a thermal separation process for producing compounds in a pure state from solutions, melts or a gaseous phase. A saturated solution is in thermodynamic equilibrium with the equilibrium solid phase at a specified temperature (and pressure). To achieve a required supersaturation cooling, solvent evaporation or vacuum can be applied, respectively. Further techniques used in industrial processes are drowning-out crystallization utilizing an anti-solvent and reactive crystallization, as for example precipitation [16].

Crystallization techniques are of key importance in the Life Science industries [17]. Because the crystal lattice is very sensitive to small changes in molecular structure of compounds, crystallization facilitates achieving high purities. Furthermore, crystallization allows providing desired product properties as particle size distributions, crystal shapes and the right forms of the solid state. If the target substance is stable at its melting temperature, crystallization can be performed directly from the melt. Otherwise, suitable solvents (or solvent mixtures) can be applied and crystallization is carried out from solution. It should be mentioned that crystallization from the vapor phase is feasible as well [15].

From an operational point of view crystallization processes can be realized batch-wise or continuously [15–18]. The decision which operation mode is the optimal one for a certain separation problem depends on a number of substance and process related parameters and on economic and environmental considerations. However, the most important information initially required are thermodynamic functions describing the phase equilibria characteristic for the specific separation problem [19].

To resolve enantiomers by selective crystallization typically batch crystallization is applied [20]. This flexible mode of operation is straightforward regarding process design and from an operational point of view. Multi-purpose and multi-product batch plants are standard in the life-science industries for the production of pharmaceuticals, flavors and fragrances, food additives and agrochemicals. However, due to possible higher productivities and more constant product qualities, currently continuous process variants are increasingly in the focus of intensive research activities. Numerous process concepts to realize continuous selective crystallization were developed [20–27]. Due to the larger complexity, often more equipment is required and the plants are usually dedicated just to one specific separation problem. Hence, it has to be evaluated for each task specifically, if the larger investment costs related to continuous operation are compensated by possible improvements in process performance.

The simplest continuously operating crystallization process concept exploits stirred tanks, which are described in analogy to the CSTR principle applied in Chemical Reaction Engineering by the Mixed Suspension Mixed Product Removal (MSMPR) approach [15,23]. It is well known, that the unavoidable broad crystal size distributions produced in mixed vessels require often a subsequent classification unit to provide crystals in a narrower size range. For this reason, there is large interest in developing and applying alternative continuous process principles.

Suitable criteria, which are capable to quantify and compare the performance of both batch-wise or continuously operated crystallization processes devoted to provide out of a mixture a specific target component *i* are the productivity, Pr_i, and the yield, Y_i. Evaluating the fed and harvested masses, $m_{i,feed}$ and m_i, these quantities can be defined as follows for a batch process occupying the facilities with a volume, V_{total}, for a time period, Δt_{Batch}:

$$Pr_i = \frac{m_i}{\Delta t_{Batch} * V_{total}} \quad (1)$$

$$Y_i = \frac{m_i}{m_{i,feed}} * 100\% \quad (2)$$

Similarly, in a continuously operated process which has reached its steady state the incoming and outgoing mass flows, $\dot{m}_{i,feed}$ and $\dot{m}_i$, need to be evaluated to quantify the performance:

$$Pr_i = \frac{\dot{m}_i}{V_{total}} \quad (3)$$

$$Y_i = \frac{\dot{m}_i}{\dot{m}_{i,feed}} * 100\% \quad (4)$$

Further performance criteria will be introduced in Section 3, which discusses more specific product properties.

2.1. Enantioselective preferential crystallization

Preferential crystallization is a method for direct crystallization of a single enantiomer out of a racemic solution. It is applicable in cases, where the chiral molecules crystallize as a conglomerate. In a conglomerate the two enantiomers are in the solid phase just mechanical mixtures, i.e. they crystallize as separate enantiopure crystals. Only such cases are in the focus of this article. Preferential crystallization is an attractive approach that allows for direct crystallization of the desired enantiomer without the need for any chiral auxiliary, which is typically required for resolving components exhibiting other types of phase equilibria. It is a kinetically controlled separation process which exploits different crystallization rates of both enantiomers in the presence of homochiral seed crystals. After seeding a racemic solution, the seeded enantiomer selectively crystallizes for a certain period. However, according to the increasing portion of the counter-enantiomer remaining in solution, at a certain time it will inevitably nucleate and contaminate the resolved product crystals. Under equilibrium conditions the crystallized product would be racemic as the initial feed solution [28,29]. Entrainment processes exploiting preferential crystallization are usually applied for smaller scales in the conventional batch mode. To enhance the performance of the “classical” isothermal process, different innovative preferential crystallization variants have been suggested in the past. They involve, amongst others, polythermal and auto-seeding strategies and alternative reactor concepts [8,22,30]. Various alternative process variants were investigated recently. “Coupled Preferential Crystallization (CPC)” [31,32] and “Coupled Preferential Crystallization and Selective Dissolution (CPCD)” [33,34] were developed to prevent undesired nucleation of the counter-enantiomer via keeping the composition of the initial solutions racemic during the entire crystallization process. Processes coupling two crystallizers increase the driving force for desired growth and reduces the driving force for unwanted nucleation, which allows for higher productivities and yields combined with an increased process robustness [22].

So-called “Simultaneous Crystallization (SC)” is an attractive option for application in larger scales. It implies the simultaneous crystallization of both enantiomers from solutions, which are, although spatially separated, in controlled connection to maintain racemic liquid phase composition. This process can be performed in batch and continuous modes and has been industrially realized, for example, for the production of (-)-menthol (Haarmann & Reimer) and an L-α-methyldopa intermediate (Merck). Various continuous enantioseparation processes utilizing different configurations of stirred tanks, tubes and fluidized bed systems have been recently described [35], reviewed [36], compared [37] and evaluated with respect to the purity control [38]. The application of fluidized bed crystallizers was highlighted [38] as well as the integration of continuous seed crystal provision to achieve stable steady state operation [35]. The fluidized bed crystallization process combines beneficial features as the size classification, a selective fines removal, a long residence time of the solid product and a short and narrow distributed residence time of the liquid phase. These features are

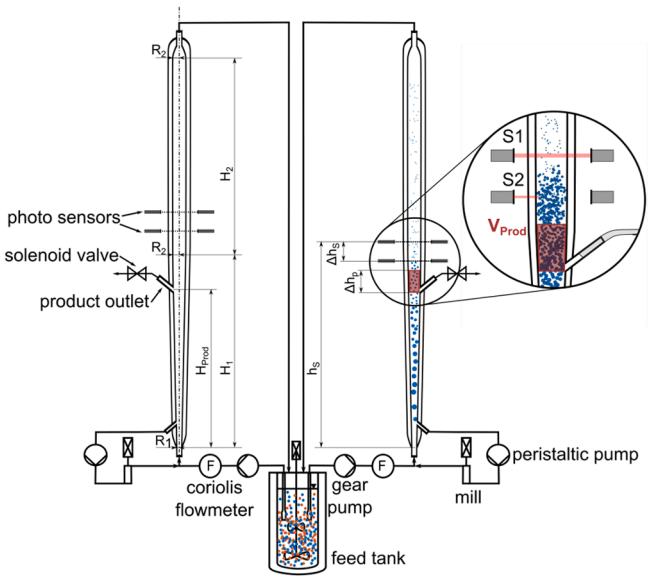

Fig. 1. Scheme of a set-up applicable for carrying out preferential crystallization in two coupled fluidized bed crystallizers to separate the two enantiomers (D and L) of a racemic (50:50) mixture introduced continuously from a feed tank. Periodic product removal is realized at each crystallizer using solenoid valves triggered by moveable photo sensors (S1 and S2). Crystallizer geometry and characteristic positions are designated in accordance with the process model introduced in Section 5.

essential for realizing a robust process for continuous enantioseparation with additionally integrated product classification. Thus, this way of performing enantioselective crystallization possesses unique advantages and is for this reason the subject of our research work reported in this article.

The benefits of using preferential crystallization were successfully demonstrated by resolving racemic calcium pantothenate and an industrially required resolving agent in both laboratory and industrial scales (35 L and 3000 L) [39,40]. More examples and information regarding the application of preferential crystallization can be found e.g. in [8,28,29].

A comprehensive summary of performance assessments reported in the literature related to continuous crystallization processes in general and applied to resolve racemic conglomerates was given recently in [41]. For the productivity (Eqs. (1) and (3)) of providing pure enantiomers from racemic mixtures a currently achievable productivity maximum of $Pr_{max} \approx 20 g/L/h$ was reported, which below will serve as a benchmark.

3. Principle of an enantioselective fluidized bed crystallization process

There is a large number of crystallization processes available and documented in the literature based on creating particles in fluidized beds. Different process principles, application examples and further references are reported. A comprehensive review is beyond the scope of this paper. Excellent instructive examples applied for wastewater treatment are given in [42–44]. Selecting from the vast literature describing precipitation and purification of inorganic salts using fluidized beds we refer exemplarily to [45,46].

The specific principle of the fluidized bed crystallization process described and investigated in this paper is capable to selectively crystallize both enantiomers of a chiral molecule out of racemic solutions in two spatially separated but connected tubular crystallizers. The concept was highlighted in [35] and discussed more recently in [22]. Results of own preliminary work, exploiting earlier variants of an experimental set-up introduced below are described in [47–49]. Here we will present both an extension of the set-up and a modification of the operating regime together with new theoretical and experimental results. A specific separation problem will be considered as a model system.

An illustration of the principle and the main features of the set-up is illustrated in Fig. 1. A racemic solution, saturated at a specific temperature, is provided in a feed tank. Crystal-free liquid phase is withdrawn from there and transported continuously via gear pumps in equal amounts through the two columns from the bottom to the top. The columns, which are connected via redirecting their upper outlets back into the feed tank, consist of a conical section in the lower part (up to H_1) and a cylindrical section in the upper part (length H_2). Thus, a liquid phase velocity profile will be develop over the height of the conical section. Hence, present crystals in this range settle downwards or are dragged upwards according to their mass in relation to the buoyancy and the drag force. At a product outlet position, which is located in the conical section (at position H_{Prod}), crystals of a specific size can be harvested. Hence, the size distribution of these product crystals is quite narrow and can be adjusted e.g. via the volumetric feed flowrate. Due to the low risk of attrition in this type of fluidized bed and the size classifying effect, it can be expected that the crystalline product will be characterized by a low fraction of fines.

The driving force required for crystallization can be provided by cooling the crystallizer jackets to a suitable temperature. Preferential crystallization can be initiated by seeding each column one time from the top with a certain amount of one of the pure enantiomers. The seeded enantiomer is subsequently selectively removed from the liquid phase due to growth of the solid phase. Hence, the liquid phase composition becomes gradually non-racemic and the probability of nucleation of the unseeded enantiomer increases during the progressing process. However, the risk of product contamination due to nucleation of the respective antipode is rather low since nuclei and small particles follow the liquid stream and are transported to the top and then out of the crystallizers back to the feed tank. There these nuclei will dissolve again. The potential for nuclei removal, together with the narrow residence time distribution of the liquid phase, improves the robustness of the process. Due to the simultaneous operation of two columns, both oppositely depleted, non-racemic liquid streams can be collected together in the feed tank. This counter-balances the composition occurring in the two crystallizers. Hence, higher supersaturations can be applied compared to uncoupled variants of preferential crystallization. To maintain long (continuous) operation, eventually solid racemic excess material needs to be added to a feed tank of finite volume.

After the process is initialized as described by seeding and if suitable flowrate conditions are chosen, the growing crystals will tend to move towards the bottom of the crystallizer or they are removed at the product outlet. In order to counter-balance the loss of solid phase via the product outlet, the largest crystals at the bottom are utilized for continuous seeding. These crystals are removed out of the crystallizer and are transported via peristaltic pumps in a bypass stream through high-speed dispersers which serve as mills (mill, Fig. 1). The resulting suspension, which contains generated particle fragments, is merged with the feed stream at the end of the bypass loop and reenters the crystallizers at the bottom again. The milled smaller particles follow the liquid stream upwards through the crystal bed where they serve as new seed material. If the growing seed crystals have sufficient time to reach a certain crystal size, they will remain in the crystallizer and sediment at the top of the crystal bed instead of being discharged with the liquid stream. Thus, the growth of the crystal bed progresses.

The product removal can be realized continuously or periodically. Due to the rather low liquid phase velocities and also related to the limited size of the plant utilized, a periodic product withdrawal strategy was developed [50] and studied in more detail in this work. Hereby, periodic product withdrawal was realized exploiting two photo sensors ($S1$ and $S2$, Fig. 1) installed in each of the two crystallizers following concepts available in literature [51] and already successfully tested in [50]. When the upper light beam is interrupted by the growing crystal

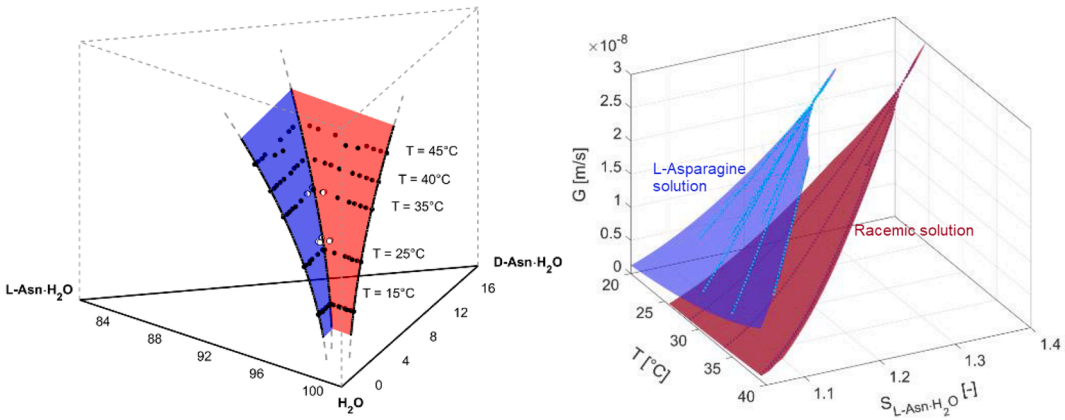

Fig. 2. Solubilities as a function of temperature in the ternary L-Asn·H_2O/D-Asn·H_2O/water system (wt%) (left). Growth kinetics of L-Asn·H_2O seed crystals from racemic and pure L-Asn solutions as functions of supersaturation, S, and temperature, T (right). (Figures adapted from [55] with permission of copyright).

bed the upper photo sensor ($S1$) triggers opening of the solenoid product valve. The product crystals located above the product outlet are withdrawn now with the surrounding liquid phase. Closing of the solenoid valve is triggered again by the lower photo sensor ($S2$) when the lower light beam can pass again. In this way a periodic operation can be realized automatically.

The essential adjustable operation parameters of the described process are the supersaturation, the crystallization temperature and the volumetric feed flowrate. The influences of these three parameters on the continuous enantioseparation were already evaluated in a preliminary experimental study [50]. A further degree of freedom is given by options for the periodic product withdrawal. In particular, the maximum height of the fluidized bed can be altered by varying the position of the upper sensor (h_S, Fig. 1). Adjusting the distance (Δh_S) between the upper ($S1$) and the lower ($S2$) sensors enables controlling the volume which is withdrawn in each cycle at the product outlet (V_{Prod}).

3.1. Further performance parameters

The productivity, Pr (Eq. (3)) can be calculated based on the crystal mass of each withdrawal step, m_i, the time window between two withdrawal steps, Δt (cycle time), and the volume of the specific crystallizer. Similarly, the yield, Y (Eq. (4)) can be calculated considering also the exploitable amount of enantiomer fed during this cycle time.

Besides considering productivity and yield, the collected solid product can be characterized by determining distributions of product crystal properties. A standard way is to describe the crystal population by a number density function, $n(L)$, which gives the number of crystals of a characteristic size, L, per volume per size (in general,n may depend on further variables like time and space coordinates; for the sake of a simple notation, this is ignored here for the moment). Number density functions are convenient quantities for modeling purposes and will be used within the process model introduced in Section 5. The cumulative mass (or volume) related size distribution

$$Q_3(L) = \frac{\int_{l=0}^{L} n(l)\cdot m(l)\cdot dl}{\int_{l=0}^{\infty} n(l)\cdot m(l)\cdot dl} \tag{5}$$

gives the mass of crystals with size L or smaller in relation to the total crystal mass, $m(L)$, being the mass of a crystal with size L. The derivative of $Q_3(L)$,

$$q_3(L) = \frac{dQ_3}{dL}(L) = \frac{n(L)\cdot m(L)}{\int_{l=0}^{\infty} n(l)\cdot m(l)\cdot dl}, \tag{6}$$

is a measure for the mass fraction of crystals of size L. Two characteristic parameters of the distribution used in the following are the mass weighted mean crystal size

$$L_3 = \frac{\int_{l=0}^{\infty} n(l)\cdot m(l)\cdot l\cdot dl}{\int_{l=0}^{\infty} n(l)\cdot m(l)\cdot dl} = \int_{l=0}^{\infty} l\cdot q_3(l)\cdot dl \tag{7}$$

and the standard deviation

$$s_{L,3} = \sqrt{\int_{l=0}^{\infty} (l - L_3)^2\cdot q_3(l)\cdot dl} \tag{8}$$

Sieve analysis can be exploited to determine the above quantities experimentally. Hereby the crystals can be grouped in N size classes, each containing crystals of size $L_k \pm \frac{\Delta L_k}{2}$, $k = 1, \ldots, N$. The size distribution, $q_3(L)$, the mean crystal size, L_3, and the standard deviation, $s_{L,3}$, can be approximately determined using

$$q_3(L_k) \approx \frac{\Delta Q_{3,k}}{\Delta L_k} \tag{9}$$

$$L_3 \approx \sum_{k=1}^{N} L_k\cdot \Delta Q_{3,k} \tag{10}$$

$$s_{L,3} \approx \sqrt{\sum_{k=1}^{N} (L_k - L_3)^2\cdot \Delta Q_{3,k}} \tag{11}$$

with the mass fraction $\Delta Q_{3,k} = Q_3\left(L_k + \frac{\Delta L_k}{2}\right) - Q_3\left(L_k - \frac{\Delta L_k}{2}\right)$.

4. Chiral system investigated and crystallization-related properties

To demonstrate and evaluate the fluidized bed separation process introduced above experimental investigations were performed with the chiral amino acid asparagine ($C_4H_8N_2O_3$, abbreviated as Asn, molar mass (anhydrous) $M_{anhydr.} = 132.12 g/mol$) and water as solvent. L-Asn is a nonessential proteinogenic amino acid, which is applied to treat low blood pressure, kidney problems, or liver damage. Asparagine crystallizes from aqueous solutions as a monohydrate (molar mass $M_{hydr.} = 150.13 g/mol$) forming in the solid phase a conglomerate [48]. DL-, L- and D-Asn·H_2O were purchased from Sigma Aldrich (Purity >99%) and were used without further treatment. The solvent for the crystallization studies was deionized water using a milli-Q system (Merck Millipore, Milli-Q Advantage).

The following thermodynamic properties characterize the two phases present during the crystallization process:

Heat capacity of the solid phase at 24 °C [52]:
$c_{p_{solid}} = 1372 Jkg^{-1}K^{-1}$
Average heat capacity of the aqueous solution:
$c_{p_{liquid}} = 4180 Jkg^{-1}K^{-1}$
Density of the solid phase at ambient temperature [47]:
$\rho_{solid} = 1540 \mathrm{kgm}^{-3}$
Average density of the liquid phase (own measurement):
$\rho_{liquid} = 1010 \mathrm{kgm}^{-3}$

Solubility and metastable zone width of the chiral molecules in water have been measured previously and are reported in [53]. Extending this study, a detailed investigation of the crystallization kinetics of the L-Asn·H_2O from both aqueous L-Asn·H_2O and DL-Asn·H_2O solutions has been carried out. The results related to quantifying the crystal growth are based on the method described in [54] and were summarized in [55].

The left side of Fig. 2 shows the ternary solubility phase diagram of L- and D-Asn·H_2O in water covering a temperature region of 15 to 45 °C. The solubilities increase with increasing temperature while the "double-solubility rule" applies, which means that the solubility of the racemate nearly doubles the one of the pure enantiomers.

The saturation concentrations expressed as mass fractions of L-Asn·H_2O and *D*-Asn·H_2O, $x_{sat,i}$, can be determined for a given temperature, T (in K), and mass fraction of the solvent, $x_{solvent}$, using Eq. (12) [55].

$$x_{sat,i} = 0.0104 + 1.058 \cdot 10^{-4} \cdot (T - 273.15) + 2.443 \cdot 10^{-5} \cdot (T - 273.15)^2 + 0.0312 \frac{x_j}{x_{solvent}}$$

i = D-Asn·H_2O, L-Asn·H_2O and j = L-Asn·H_2O, D-Asn·H_2O ($j \neq i$), T in K (12)

From the temperature dependence of the solubilities the weight based crystallization enthalpy can be estimated by applying the equation of Schröder-Van Laar [28] to be $\Delta H_{cryst} = -229 kJkg^{-1}$.

The determined growth kinetics of L-Asn·H_2O from aqueous L-Asn and DL-Asn solutions are shown in Fig. 2 (right). Whereas for solubility equilibria almost ideal solution behavior of the enantiomers in water is observed, the crystal growth kinetics reveal a significant difference, if the counter enantiomer is present. The growth rates in enantiopure solution exceed those in racemic solution over the entire region of supersaturations and crystallization temperatures studied. The growth rate, G_i, for a given supersaturation, $S_i = x_i/x_{sat,i}$, and temperature, T, can be calculated for the system considered with Eq. (13) [55].

$$G_i = k_g \cdot (S_i - 1)^{n_g} \exp\left(-\frac{E_g}{RT}\right) \quad (13)$$

with $k_g = 8.43$ x10^6 ms^{-1}, $n_g = 2.47$, $E_g = 76.74$ kJmol^{-1} i = D-Asn·H_2O, L-Asn·H_2O

The above given properties will be used in the following sections, first as input data for process modeling and simulations (Section 5) and then for designing and interpreting experiments (Section 6).

5. Process model and simulations

In this section we will introduce a 1D model of the process described, which will be used to evaluate the sensitivity of essential parameters. Simulation studies will illustrate the periodic product withdrawal strategy and describe the impact of the crystallizer geometry.

5.1. Objective and model assumptions

The described coupled continuous crystallization process has many degrees of freedom for process design. Due to the rather small operation window, the free operation and design parameters have to be chosen with care. Process design and optimization based on experimental studies alone would hardly be feasible. Instead, a process model is needed that, on the one hand, is sufficiently detailed to capture the effects of all relevant design parameters. On the other hand, the numerical effort needed to solve and optimize the model equations should not be too high. Models, which offer a reasonable compromise between these conflicting objectives, have been published in [47,56–59]. It could be shown that these models describe the interaction between crystal growth, particle transport, and fluid dynamics in the isothermal case with reasonable accuracy. The process model presented in the following is based on [57,59] and refines several aspects of the existing models. The model distinguishes between the L-and the D-enantiomer. This allows to evaluate not only the productivity but also the purity of the withdrawn product. It is well known that crystallization kinetics crucially depend on the temperature [15]. Thus, following [60], the extended model accounts for this by adding besides the mass balances an additional energy balance equation.

The process model is based on the following main assumptions (for further details, see [59]). The crystal population is described by a number density function that depends on a single space coordinate h in direction of the liquid flow, a single property coordinate L representing a characteristic crystal size, and on time t. Plug flow conditions are assumed for the liquid. The particle velocity, which differs from the liquid velocity, is described by the classical model by Richardson and Zaki [61], using a sphericity parameter φ [47] for the discrepancy between the movement of the crystals in the liquid and the movement of spherical particles with the same volume. Similar to [62], the proposed model considers a perfectly symmetric system in terms of crystal formation mechanisms and their rates. The only asymmetry between the two enantiomers comes from the initial conditions. Crystal growth is modeled by experimentally validated kinetics [55]. Nucleation kinetics of a similar structure as the growth kinetics are assumed in order to assess the purity of the product. Instead of assuming a constant product flowrate as in [59], the pulse-wise periodic withdrawal of product crystals is modeled. As a simple model of the disperser, we use a standard population balance model with breakage, similar to the model of a screen mill described in [63]. Other models which describe milling processes can be found in [64].

A challenging aspect is the modeling of the described pulse-wise product withdrawal. The objective here is to find a simple, yet sufficiently precise description for taking a segment of the fluid periodically out of the crystallizer. At first, the triggering of the upper photo sensor ($S1$, Fig. 1) has to be modeled. It is assumed that the product withdrawal is initiated by the volume fraction of the liquid phase (Eq. (A.9)) at the sensor position h_s falling below a pre-specified value $\in_{desired}$. The sensitivity of the modeled sensor can be adjusted by varying the parameter $\in_{desired}$. The next step is to describe the withdrawal of the suspension segment. In the model, this is assumed to happen instantaneously, i.e. the suspension located within Δh_p above the product outlet, H_{Prod}, is taken out and forms the harvested product. The removed volume of Δh_p is equal the volume between both sensors, Δh_S.The suspension above

Table 1
Parameters of the "Reference case" used in the simulations with the 1D model (according to the equations summarized in Appendix A). The position of the upper photo sensor, h_S, is indicated as the distance to the position of the product outlet, H_{Prod} (which varies slightly for each crystallizer).

Operating parameters		
Crystallization Temperature	T_{cryst}	30 °C
Saturation Temperature	T_{sat}	35 °C
Liquid phase inlet concentrations	$c_{in}^{L} = c_{in}^{D}$	0.0454 $kg_{solute} kg_{solution}^{-1}$
Volumetric feed flowrate	$\dot{V}_{in}$	12 Lh^{-1}
Parameters of the periodic product withdrawal		
Upper sensor position	$h_S - H_{prod}$	0.155 m
Distance between both sensors	Δh_S	0.120 m
Desired fraction of fluid at h_s	$\epsilon_{desired}$	0.9

$H_{Prod} + \Delta h_p$ just moves downwards over the length Δh_p. In a last step, the top part of the crystallizer, which is now empty in the model, has to be refilled. This is done by filling up the empty top segment of the crystallizer with pure liquid possessing the inlet composition. Assuming that there are hardly any crystals in the top part of the crystallizer is a reasonable assumption, which is confirmed by the simulations. Choosing the right liquid composition in the crystallizer top part is more difficult, and the assumptions made may deviate from reality. However, due to the plug flow like behavior, the liquid composition at the top has a negligible effect on the overall behavior of the crystallizer.

The complete set of model equations, additional parameters and information regarding the numerical solution are provided in Appendix A.

5.2. Simulation results and parameter study

5.2.1. Simulation of the reference case

A first set of calculations was performed for a "Reference case". The corresponding operating parameters, temperatures, inlet concentration, volumetric feed flowrate and sensor positions, were chosen in agreement with the successful preliminary experimental study [50]. They are listed in Table 1. The value of the liquid fraction $\epsilon_{desired}$ at the sensor position h_S was selected in accordance with visual observations made in the experiments.

The required physical–chemical model parameter values are available from previous studies [52,55] as summarized in Section 4. Parameters related to the performance of the mill and heat transfer coefficients were estimated as described in Appendix A and are summarized in Table A1.

In a first attempt, this "Reference case" was simulated for the two crystallizers used in the previous experimental study [50]. Hereby, the slightly differing geometrical parameters are specific for each crystallizer as listed in Appendix B (Table B1). The slight deviations are due to unavoidable small differences in manufacturing the two glass vessels. These two crystallizers are designated below as Cref-D and Cref-L, to designate the specific enantiomer seeded and produced.

Fig. 3shows simulation results of the "Reference case" for Cref-L after reaching the cyclic steady state. Shown are four snapshots of the particle number size density at different time instants of one operation cycle. The upper left one shows the crystal distribution immediately before the product withdrawal. One can see that the fluidized bed just reaches up to the sensor, h_S. Above the sensor, the fluid is nearly crystal free. Product is withdrawn when the volume fraction of the liquid at the sensor position falls below the specified value $\epsilon_{desired}$ that triggers the sensor. The upper right diagram contains the crystal distribution immediately after the product withdrawal. The crystals bed above $H_{Prod} + \Delta h_p$ has dropped at this instant by $\Delta h_p \approx 0.13$ m.

The lower left diagram shows the crystal distribution roughly in the middle of the periodic cycle. Gradually, crystals of medium size accumulate again in the vicinity above the product outlet position, Δh_p. Finally, the lower right diagram contains the crystal distribution immediately before the next product withdrawal. The duration of the cycle, Δt, for this "Reference case" is equal to 1.7 h. Each product withdrawal causes crystals located above the withdrawal point to move instantaneously downward, thus remaining in the crystallizer.

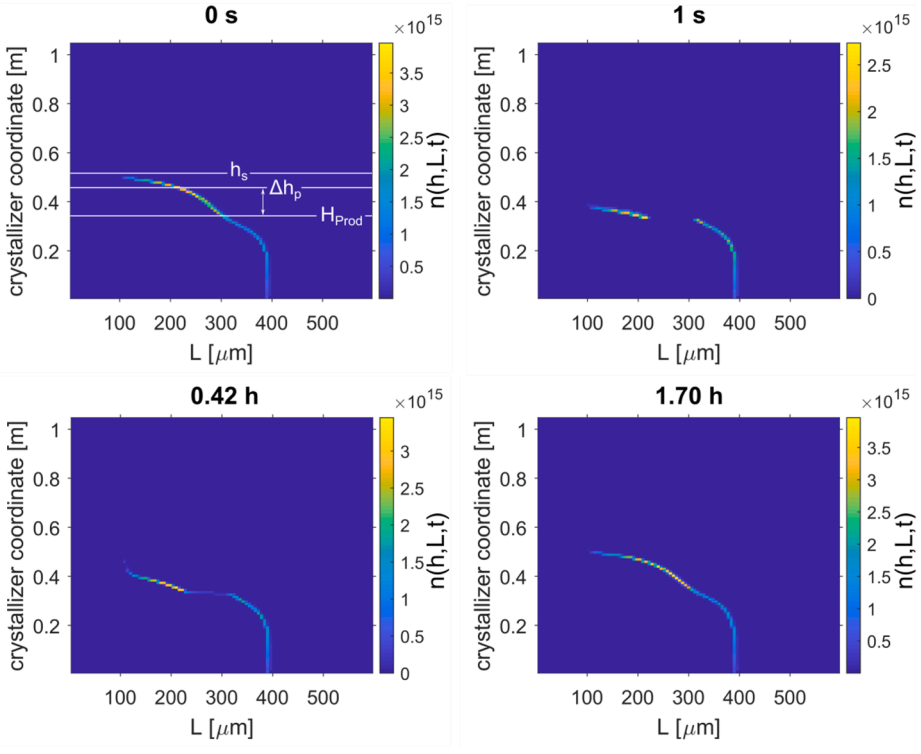

Fig. 3. Simulated number size densities $n(h, L, t)$ for the parameters corresponding to the "Reference case" and the crystallizer Cref-L. The figure shows four snapshots illustrating the location of different sizes of crystals within the crystallizer covering a period of 1.7 h: Immediately before product removal, immediately after product removal, at a later time point during the cycle, and finally at the end of the cycle (right before the next product removal). Model equations in Appendix A. Parameters in Section 4, Table 1 and Appendix A (Table A1).

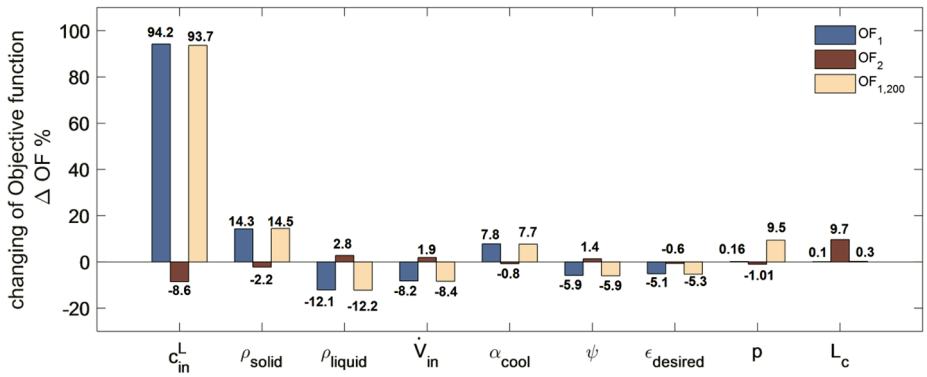

Fig. 4. Results of sensitivity analysis for the "Reference case" (considering Cref-L, parameters presented in Section 4, Table 1 and Appendix A Table A1). The parameters are ordered according to the magnitude of their effect on the objective function OF_1. Objective Functions OF_1 (Eq. (15)); $OF_{1,200}$ (Eq. (16)), for crystals larger than$x = 200\mu$m), OF_2(Eq. (17)).

5.2.2. Process sensitivity with respect to essential model parameters

The relevance of the model parameters was studied performing a local sensitivity analysis. The objective of the study was two-fold. On the one hand, the analysis was made to help identifying which model parameters have to be adjusted carefully to measurements, and for which parameters rough estimates are good enough in order to obtain a predictive model. On the other hand, the sensitivity study helps to find out, which operation and design parameters have a strong effect on the key performance parameters as productivity, yield, and particle size (Eqs. (3), (4) and (7)).

To assess the parameter influences, a normalized sensitivity function was used that is defined as the approximate percentage change in an objective function for a fixed change in a certain parameter, p_j. As a fixed change, an increase of 10% in each parameter studied was evaluated, keeping all other parameters constant. This leads to the following definition of the sensitivity S_{kj} used:

$$S_{kj} = \left.\frac{\Delta OF_k}{\Delta p_j}\right|_{k\neq j}, \quad where\ \Delta p_j = p_j^{nominal} - p_j = 0.1 p_j^{nominal} \tag{14}$$

In the above formula, OF_k is the process performance parameter or objective function under consideration. The following objective functions were considered:

$$OF_1 = Pr \tag{15}$$

Thus, this objective function is the mass based productivity defined in Eq. (3). If only crystals larger than a specific threshold size x are considered another objective function can be determined:

$$OF_{1,x} = Pr_x \tag{16}$$

Furthermore, it is instructive to evaluate the mean crystal size (Eq. (7)):

$$OF_2 = L_3 \tag{17}$$

Another objective function, which also evaluates fractions of larger crystals in the product, will be discussed in Section 7 in the context of a more detailed model of the crystallizer.

In order to evaluate the influence of relevant parameters on process performance a normalized sensitivity is instructive.

$$S_{kj}^{norm} = \frac{\Delta OF_k}{\Delta p_j} \Big/ \frac{OF_k^{ref}}{p_j^{ref}} \tag{18}$$

Normalized sensitivities are illustrated in Fig. 4 for the three objective functions given in Eqs. (15)–(17). Keeping the standard parameters of the "Reference case", the following parameters are evaluated individually: a) particle density, ρ_{solid}, fluid density, ρ_{liquid}, and particle sphericity, Ψ, because they affect the movement of the crystals in the liquid; b) the screening size of the mill, L_c, and the number of daughter crystals created during breakage in the mill, p, because they determine the amount and the size of the seed crystals; c) the heat transfer coefficient between crystallizer and coolant, α_{cool}; d) the liquid volume threshold fraction $\epsilon_{desired}$ as measure for triggering the light sensor (Eq. (A.9)); and finally as adjustable operating parameters, e) inlet concentration, c_{in}^{L}, and volumetric feed flowrate, $\dot{V}_{in}$. Among these parameters, the inlet liquid concentration, $c_{in}^{D} = c_{in}^{L}$, was found to have the strongest effect on the chosen objective functions, which is not surprising, because it immediately changes the supersaturation of the solution. The volumetric feed flowrate determines for given fluid and solid density the movement of the crystals relative to the liquid flow. Fig. 4 shows that the

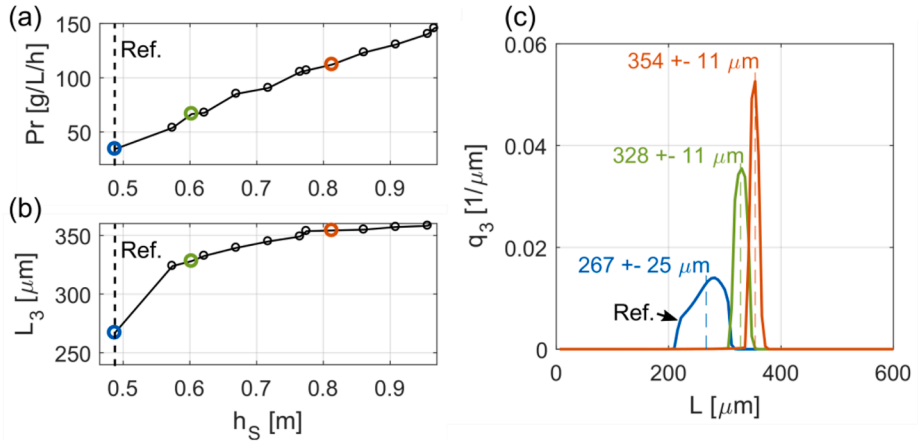

Fig. 5. Influence of the upper sensor position, h_S, on a) the productivity, Pr (Eq. (3)), b) mean product crystal size, L_3 (Eq. (7)), and c) the product crystal size distribution, q_3 (Eq. (6)), with their respective mean values and standard deviations. Three product crystal size distributions are given for the sensor positions, h_S (blue, 0.488; green, 0.603; red, 0.813 m). The sensor position,h_S, of the "Reference case" is indicated (Ref.). The height of the withdrawn segment (Δh_p, Fig. 1) is equal 85 mm for all simulations. Shown simulation results correspond to crystallizer Cref-L. (For interpretation of the references to colour in this figure legend, the reader is referred to the web version of this article.)

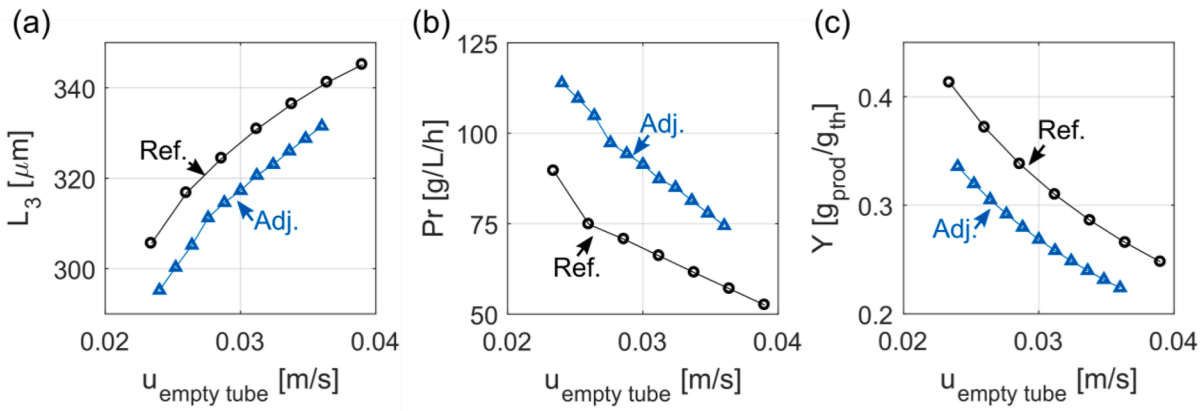

Fig. 6. Simulation results of the "Reference geometry" (i.e. Cref-L, black rings) and the "Adjusted geometry" (i.e. Cadj-L, blue triangles). Given are a) the mean product crystal size, L_3 (Eq. (7)), b) the productivity, Pr (Eq. (3)), and c) the yield, Y (Eq. (4)), as a function of the empty tube velocity (Eq. (A.8)). Parameters of the withdrawal strategy were chosen in accordance to the experiments evaluated below in Section 6, $h_S - H_{Prod} = 0.265m$ and $\Delta h_p = 0.085m$. (For interpretation of the references to colour in this figure legend, the reader is referred to the web version of this article.)

solid and fluid density affect the productivity and crystal size even stronger than the volumetric feed flowrate. Hence, these physical properties have to be accurately chosen by measurements. The liquid fraction $\in_{desired}$ is a measure for the sensitivity of the upper sensor ($S1$, Fig. 1), which triggers the product removal. It has also a significant effect on the three objective functions. The critical length of the crystals selected, L_c (Eq. (A.12)), hardly changes the productivity, but can clearly be used to adjust the mean product crystal size.

The results shown in Fig. 4 are considered to be helpful for selecting sensitive variables for a numerical process optimization, which is subject of our future work.

5.2.3. Model based analysis of the influence of the sensor positions

After specifying a separation problem, the crystallizer geometry and suitable operating parameters are of key interest. Before considering the effect of the former, in this section we will focus on the product withdrawal strategy, in particular the position of the upper sensor, h_S. This position is crucial for the finally established periodic operation regime. It can be varied with moderate effort.

When the sensor position h_S is lifted up above the position of the "Reference case" (Table 1), it is observed that the time between two withdrawals decreases. This corresponds to a higher harvesting frequency increasing the productivity, Pr (Fig. 5a). Also the simulated mean product crystal size, L_3 (Eq. (7)), depends on the sensor position (Fig. 5b). One can see that a higher sensor position tends to generate larger product crystals, although the effect on the mean crystal size is not as strong as on the productivity. As the product crystal size is important for many applications, it is worthwhile having a closer look on the crystal size distribution for different sensor positions. Fig. 5c depicts the product crystal size distributions for three different sensor positions. As can be seen, for higher sensor positions, the product crystal size distribution is favorably sharpened and moves towards larger product crystals, which should be preferable in most applications. The sensor position is of course limited by the maximal height of the crystallizer.

From the simulation results presented, it can be concluded that the sensor triggering the product withdrawal should be preferably placed at high positions.

5.2.4. Model based analysis of the influence of the crystallizer geometry

In a previous study, another model was already used to compare two different crystallizer geometries [59]. The geometry discussed above corresponds to the two crystallizers of the previous experimental study [47,50] (introduced as Cref-D and Cref-L). It will be designated below as "Reference geometry". In [59] a modified crystallizer geometry (below designated as "Adjusted geometry") was suggested for higher productivity. This "Adjusted geometry" has a larger opening angle, a larger diameter of the cylindrical section and a shorter total height. The geometrical parameters of the two newly manufactured crystallizers with "Adjusted geometry" (designated below as Cadj-D and Cadj-L) are provided in Appendix B (Table B1).

A comparison of the two geometries based on simulation results using again the model introduced in Section 5 is shown in Fig. 6. The essential modified parameter was the volumetric feed flowrate, expressed as the empty tube velocity (Eq. (A.8)). To allow for correct operation, this has to be in different ranges for the two different geometries

Table 2
Features of the seven runs conducted. Varied process conditions are the crystallizer geometry, the volumetric feed flowrate, $\dot{V}_{in}$, and the product withdrawal strategy. The latter is defined by the distance between both photo sensors, Δh_S, and the position of the upper photo sensor h_S. (Fig. 1) indicated as the distance to the position of the product outlet, H_{Prod} (which varies slightly for each crystallizer). Each listed operating point was generated within both crystallizers of the pilot plant (except for Run 3 where dissimilar Δh_S were applied for the two crystallizers with "Adjusted geometry", Cadj-D and Cadj-L). In all runs the crystallization temperature, T_{cryst}, was 30 °C and the saturation temperature, T_{sat}, 35 °C.

Goal of experiments	Run	Crystallizer geometry	$\dot{V}_{in}$ [L/h]	Withdrawal strategy		
				$h_S - H_{Prod}$ [m]	Δh_S [m]	
Study of periodic product withdrawal strategy	1	reference	12	0.155	0.120	
				0.265	0.066	
				0.435	0.066	
	2	reference	12	0.155	0.120	
				0.435	0.066	
				0.635	0.066	
Periodic product withdrawal strategy for adjusted crystallizer geometry	3	adjusted	25.6		Cadj-D	Cadj-L
				0.155	0.120	0.120
				0.265	0.075	0.230
				0.355	0.075	0.320
Influence of the crystallizer geometry	4	adjusted	21.6 26	0.265	0.075	
	5	adjusted	26 30.3	0.265	0.075	
	6	reference	10 12	0.265	0.066	
	7	reference	12 14	0.265	0.066	

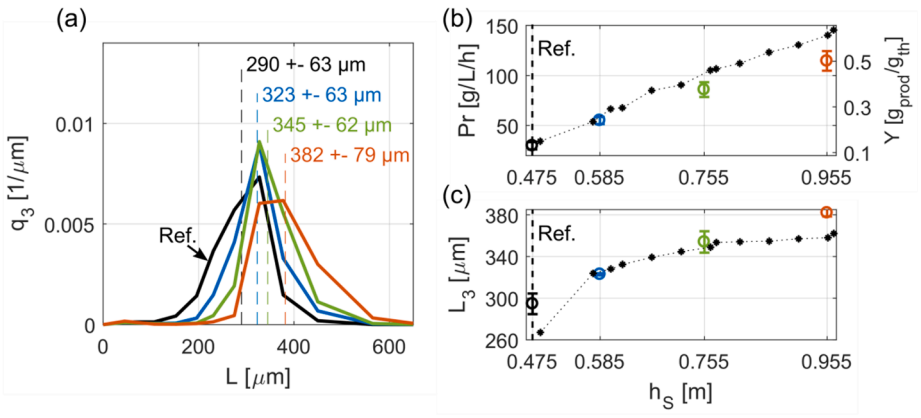

Fig. 7. Mean steady-state crystal size distributions, q_3, (Eq. (9)) with their respective mean values and standard deviations (a), productivities, Pr, yields, Y (b), and mean product crystal size, L_3 (c), for four different product withdrawal strategies, which mainly differ regarding the position of the upper photo sensor, h_S (black, 0.475; blue, 0.585; green, 0.755; red, 0.955m). The distance between both photo sensors is $\Delta h_S = 0.066m$ (except for the "Reference case", $\Delta h_S = 0.120m$, black). Given results are from Cref-D (Runs 1, 2). Theoretical results corresponding to the process model (Section 5.2.3.) are given as dotted lines in (b) and (c). (For interpretation of the references to colour in this figure legend, the reader is referred to the web version of this article.)

A larger empty tube velocity results in larger product crystals, albeit at the price of reduced productivity and yield. It was found, as already mentioned in the previous study [59], that the "Adjusted geometry" should be capable of improving the performance in terms of productivity. More specifically, for the "Adjusted geometry" slightly smaller crystals are provided combined with higher productivity and lower yield. Based on these theoretical results, experimental investigations with the "Adjusted geometry" were planned and realized.

6. Demonstration of enantioselective fluidized bed crystallization

As mentioned above results of a preliminary experimental study of the process were available evaluating the influence of supersaturation, crystallization temperature and volumetric feed flowrate [50]. The results of this study also confirmed, that steady-state operation can be reached and the separation results were very well reproducible. Based on the theoretical results reported in the previous section, new systematic separation experiments performed in the course of the current study were focused on investigating more specifically the influence and the potential of the periodic product withdrawal strategy (Section 6.2) and the crystallizer geometry (Section 6.3). These experiments were also performed to validate the process model introduced in Section 5.

6.1. Procedures and preliminary separation experiments

Altogether seven separation experiments were carried out (Runs 1–7) applying identical procedures and using the same analytical techniques as in [50] (see Appendix C). Table 2 lists the essential features of these experiments along with the specific process conditions.

The series of Runs 1 and 2 were directed to study the influence of the product withdrawal strategy. This strategy is defined by two process conditions. First, by the position of the upper photo sensor (h_S, Fig. 1), which is equal to the maximal height of the fluidized bed. Second, by the distance between both photo sensors (Δh_S, Fig. 1), and thus, the volume withdrawn per cycle. The withdrawal strategy of the previous study ("Reference case", [50]) is defined by $\Delta h_S = 0.120m$ and $h_S - H_{Prod} = 0.155m$ (see Table 1). This strategy was tested as first operation point of Runs 1 and 2, after which a good agreement with [50] was found. Subsequently, new positions of the two photo sensors were tested. In particular, the height of the upper photo sensor, h_S, was increased stepwise, to alter hereby the height of the crystal bed. Preliminary experiments increasing Δh_S caused unbeneficial effects in terms of process performance and process robustness. Consequently, Δh_S was reduced to $0.066m$.

To investigate the influence of the crystallizer geometry, Runs 3, 4 and 5 were conducted in two new specially manufactured crystallizers, which exhibit the above mentioned "Adjusted geometry" (Section 5.2.4). These adjusted crystallizers, designated as Cadj-D and Cadj-L, differ from the crystallizers with "Reference geometry", designated as Cref-D and Cref-L, with respect to the opening angles of the conical sections and the heights and radii of the cylindrical sections. The measured dimensions of all four crystallizers are provided in Appendix B (Table B1).

Besides testing the new "Adjusted geometry", the series of Run 3 was conducted to test the new pair of crystallizers applying different product withdrawal strategies. As the best compromise between productivity and robustness was found $h_S - H_{Prod} = 0.265m$ *and* $\Delta h_S = 0.075m$, which then was used in the next runs.

Runs 4–7 aimed to compare the "Reference geometry" and the "Adjusted geometry" and to evaluate, whether the "Adjusted geometry" has really the potential to improve the productivity. Since the size distribution of the crystals fluidized influences the productivity [50], it was intended to compare both geometries at similar product crystal sizes. Thus, the volumetric feed flowrates were adjusted appropriately to achieve in both geometries similar empty tube velocities of the liquid phase at the height of the product outlet, H_{Prod} ($u_{empty\ tube}$, Eq. (A.8)). Therefore, the series of Runs 4 and 5 were conducted at $\dot{V}_{in}$=21.6, 26.0 and 30.3L/h in the crystallizers with "Adjusted geometry", Runs 6 and 7 respectively at $\dot{V}_{in}$=10, 12 and 14L/h in the crystallizers with the "Reference geometry".

The achievement of high purity of the solid product harvested, which is the first essential process goal of enantioseparations, was checked by high performance liquid chromatography (HPLC) using a selective chiral stationary phase. The solid phase identity was confirmed applying X-ray powder diffraction (XRPD). A summary of the analytical methods used is given in Appendix C.

6.2. Influence of parameters of the product withdrawal strategy

The periodic product withdrawal strategy is defined by two process parameters, the position of the upper photo sensor (h_S, Fig. 1) and the distance between both photo sensors (Δh_S, Fig. 1). The influence of the first mentioned parameter, h_S, is discussed in the following Section 6.2.1. The observed influences of the second parameter, Δh_S, are presented in Section 6.2.2.

6.2.1. Influence of bed height and upper sensor position

Along the first two experiments (Runs 1 and 2, Table 2), four operation points were investigated at their cyclic steady-state. These four operation points mainly differed regarding the position of the upper photo sensor, h_S, and thus differ regarding the height of the fluidized crystal bed. Fig. 7 depicts for each strategy the mean product crystal size distribution with their respective mean values and standard deviations (a), the steady-state productivities and yields (b), and the steady-state mean product crystal size (c).

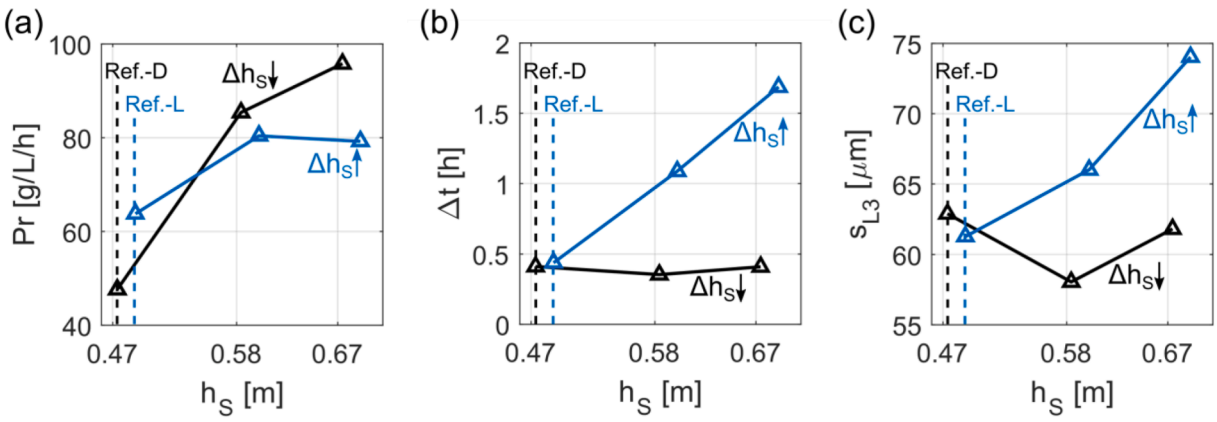

Fig. 8. Productivity, *Pr* (a), time window between two withdrawals, Δt (b), and standard deviation of the product crystal size distribution,s_{L3} (c), over the position of the upper photo sensor, h_S. The results are from Run 3 for Cadj-L (blue triangles), where the distance between both photo sensors, Δh_S, increases with h_S, and for Cadj-D (black triangles), where Δh_S decreases with h_S. The "Reference case" conducted within both crystallizers is indicated as dotted lines. (For interpretation of the references to colour in this figure legend, the reader is referred to the web version of this article.)

As shown in Fig. 7a and c, the product crystal size increases significantly with increasing crystal bed height, from 290 to 323 and 345 to 382 μm. One reason is that with increasing crystal bed height, the residence time of the product crystals increases. For the conditions of the "Reference case", almost all crystals above the product outlet are withdrawn. Consequently, the residence time of the product crystals, after they started to settle, is approximately one cycle time. This differs from the strategy with highest crystal bed, where the residence time of the settling product crystals could be five times the cycle time or even more. Thus, the crystals have more time to grow which results in larger product crystals. Consequently, the local void fractions are decreasing due to force balance and the fluidized bed gets more compact. At the largest crystal bed height and thus lowest void fraction, the standard deviation of 79 μm is significantly higher than at the other crystal bed heights. This observation leads to the assumption that the void fraction influences the movement of the fluidized crystals and thus the dynamics and the selectivity of the size classifying effect.

As depicted in Fig. 7b, the crystal bed height shows strong improvements in terms of productivity and yield. In particular, the productivity of the "Reference case" ($Pr = 30-40 g/L/h$, confirming [50]) was doubled or even tripled by increasing the crystal bed height. An explanation for the increase is that despite the presence of larger particles the overall crystal surface and, thus, the overall crystallization rate is increased through the enlarged crystal number within the higher and more compact crystal bed. Further, the enlarged number of crystals, which grow and move towards the milling bypass, results in an enlarged number of seed crystals and hence, accelerate the preferential crystallization of the target enantiomer.

Unwanted nucleation of the counter enantiomer was observed after short operation time during Run 2 with the largest crystal bed height. Increased nucleation probability can be attributed to the selective depletion of the feeding solution, i.e. the yield (Fig. 7b). Hence, the process is limited by an exploitable upper border with respect to h_S.

As predicted by the simulations described in Section 5 the periodic product withdrawal strategy, in particular the height of the fluidized bed, have a significant influence on the resulting product crystal sizes and provide a large potential to optimize the process productivity. In this particular case study, productivities of up to 90 g/L/h were reached (Fig. 7b), which is far above the before mentioned benchmark value of 20 g/L/h (Section 2.1).

6.2.2. *Influence of the distance between the two sensors*

It was observed in preliminary experiments that increasing the distance between the two photo sensors, Δh_S, and, thus, collecting with lower frequency in each withdrawal step larger volumes, did not offer beneficial effects in terms of process performance and robustness. This trend was further evaluated in Run 3, where different sets of Δh_S and h_S were tested. As a function of h_S are shown in Fig. 8: (a) the obtained

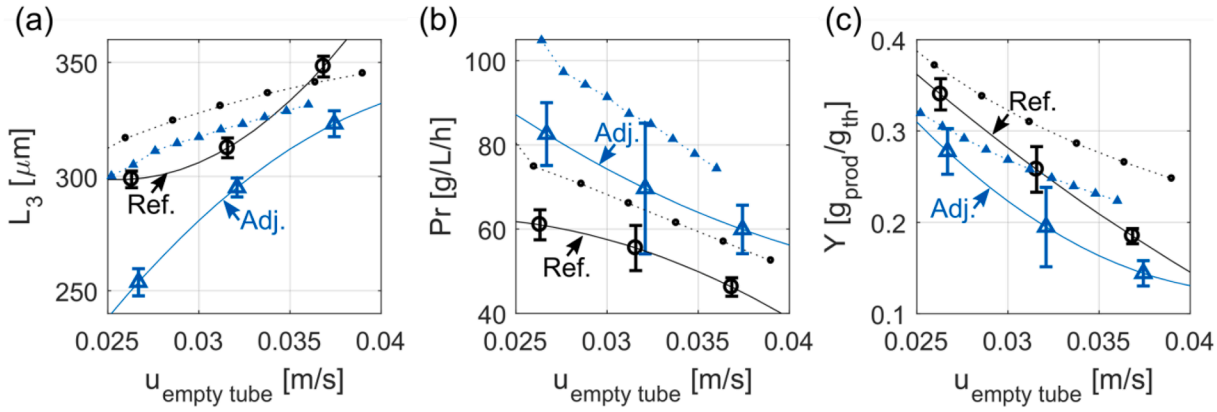

Fig. 9. Mean product crystal size, L_3 (a), productivities, *Pr* (b), and yields, *Y* (c), over the empty tube velocity at the height of the product outlet, $u_{empty\ tube}$ (Eq. (A.8)). Given are results for Cref-L with "Reference geometry" (Runs 6 and 7, black rings), and for Cadj-L with "Adjusted geometry" (Runs 4 and 5, blue triangles). The results of the process model (see Fig. 6) are depicted for both geometries as dotted lines. (For interpretation of the references to colour in this figure legend, the reader is referred to the web version of this article.)

productivity, *Pr*, (b) the time interval between two withdrawals, Δt, and (c) the standard deviation of the product crystal size distribution, s_{L3}. For the crystallizer Cadj-L (blue data), Δh_S increases with h_S, whereas for the crystallizer Cadj-D (black data) Δh_S decreases with h_S.

As visualized in Fig. 8a, the *Pr* increases with h_S as reported in previous sections (Sections 5.2.3 and 6.2.1.) although the productivity enhancement is for Cadj-L lower than for Cadj-D with reduced Δh_S. The origin for this can be explained considering Fig. 8b. The time interval between two withdrawals increases significantly with Δh_S due to the enlarged accumulations of the crystal bed. These enlarged accumulations reduce the time averaged crystal number and crystal surface, which causes a lower *Pr*. A further influence can be seen in Fig. 8c. The product crystals produced at high Δh_S exhibits significant broader crystal size distributions. Thus, the enlarged withdrawn volume counteracts the selectivity of the size classifying effect. Another unwanted effect of an increased Δh_S is related to process robustness. If a volume of certain size is withdrawn in a short period of time, the level of the solution drops in the tubular crystallizers. The subsequent evaporation of the solvent film at the crystallizer walls could cause nucleation of the counter-enantiomer and, thus, reduce the purity.

In summary, Δh_S, i.e. the distance between the two sensors, should be within the range of practical feasibility kept as small as possible to improve the process in terms of productivity, width of product crystal size distribution and process robustness. The limit situation of $\Delta h_S = 0$ corresponds to a fully continuous product withdrawal, connected with a minimal continuous outlet suspension flowrate. Such small two-phase flows are difficult to realize and control.

6.3. Influence of crystallizer geometry

To compare the two crystallizer geometries studied theoretically in Section 5.2.4. and to further prove the optimization potential, both crystallizer geometries were investigated at different volumetric feed flowrates. Therefore, Runs 4 and 5 studied the "Adjusted geometry" (larger opening angle/shorter cylindrical section) at $\dot{V}_{in} =$ 21.6, 26.0 and 30.3 L/h and Runs 6 and 7 the "Reference geometry" at $\dot{V}_{in} =$ 10, 12 and 14 L/h. As described before, these volumetric feed flowrates assure, that both geometries operated at the same range of empty tube velocities

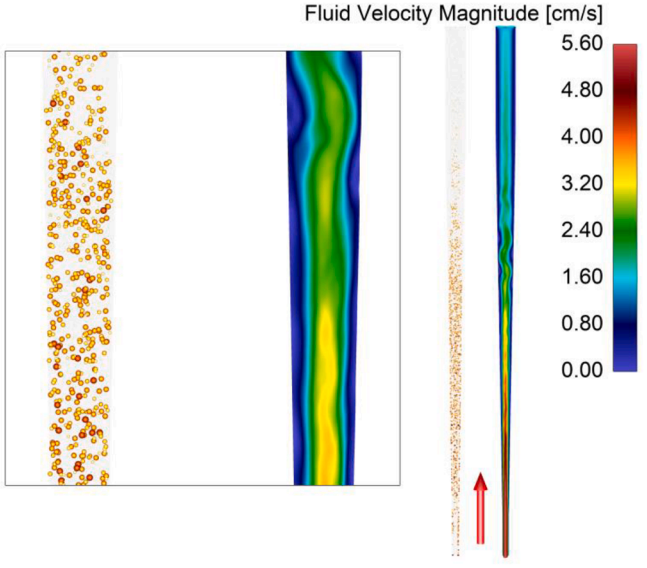

Fig. 10. CFD-DEM computational results for one of the crystallizer geometries after 60 s physical time. Left: Crystal particles resulted from the DEM simulation scaled according their size (magnified for better visibility.) Darker colors represent larger crystal sizes. Right: Liquid flow velocity magnitude obtained from the CFD simulation.

at the height of the product outlet, $u_{empty\ tube}$ (Eq. (A.8)). Fig. 9 depicts the obtained steady-state mean crystal sizes (a), steady-state productivities (b) and steady-state yields (c) over $u_{empty\ tube}$ for both crystallizer geometries.

As shown in Fig. 9a, the new crystallizers with "Adjusted geometry" produce significantly smaller product crystals evaluating situations with similar empty tube velocities at the product outlet position. Evaluating the empty tube velocities along the whole crystallizer height leads to an explanation for these smaller product crystals. At the crystallizer inlet, the empty tube velocity of the "Adjusted geometry" is 17% lower than that of the "Reference geometry" despite the higher volumetric feed flowrates. Thus, the critical crystal size for the comminuting bypass is smaller for the "Adjusted geometry", which consequently affects the whole crystal population. Regarding the classifying effect, there was no apparent trend of the standard deviations. All values scatter in a common range of 49–73 μm. However, both crystallizer geometries yield solid product with exceptional narrow crystal size distributions compared to stirred crystallizers.

As illustrated in Fig. 9b, in agreement wit the expectations, the "Adjusted geometry" provides consistently higher productivities than the crystallizers with "Reference geometry" operated at same empty tube velocity. It can be assumed that a reason for this higher productivity is the presence of significantly smaller fluidized crystals characterized by a larger specific crystal surface. Considering this, one can compare both geometries at same crystal size. Such a comparison shows for product crystal sizes of 300 μm that the productivity of the "Adjusted geometry" is $Pr = 70\,\mathrm{g/L/h}$ and, thus, slightly higher than the corresponding one of the "Reference geometry", $Pr = 60\,\mathrm{g/L/h}$. The obtained yields within the "Adjusted geometry" for the same crystal size is 20% and hence significantly smaller than the respective one of the "Reference geometry" (35%). The lower exploitation of the solution can be attributed to the higher feed throughput of the "Adjusted geometry".

In summary, the comparison shows that for a desired product crystal size the crystallizers with the "Adjusted geometry" achieve higher productivities with lower yields. Operation at lower yields provides improved process robustness, since the selective depletion of the feeding solution increases the nucleation probability of the unwanted enantiomer.

From the results shown in Figs. 7 and 9 it can be furthermore concluded, that the rather simple model introduced in Section 5 is well capable to describe the most essential process features on a qualitative and partly quantitative basis and helps identifying suitable operating conditions. However, Fig. 9 also reveals model deficits. To overcome them there are various strategies available to further improve the agreement between simulation and reality. One possibility is to identify the values of uncertain parameters from the measurement data. As the number of uncertain model parameters is quite high and the model with only one space and one property coordinate is rather complicated (the discretized model consists of about 20,000 ordinary differential equations), this is a non-trivial task. It is expected that after an improved parameter identification, the process model will be a reliable tool for process optimization and control. Nevertheless, one must concede that in the model used the fluid dynamics of the process are not considered in detail. A thorough understanding of the interactions between liquid flow and particle movement, which is a pre-requisite for more reliable optimizations of the crystallizer geometry, requires a more detailed model. Such a model is introduced and applied in the following section.

7. CFD-DEM-based geometry optimization

The strength of the discussed one-dimensional simulations based on the reduced model described in Section 5 is the associated short computational time, which is compatible with the requirement of process control. However, an obvious limitation is that the results do not provide detailed information about the hydrodynamics and the CSD.

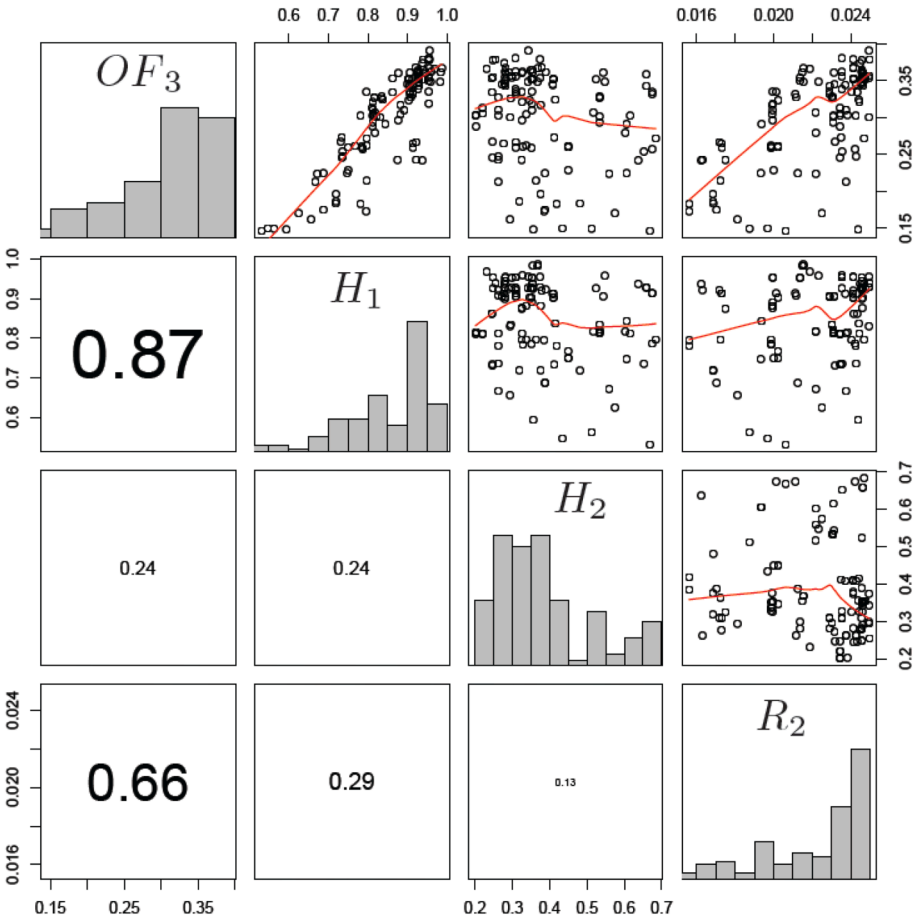

Fig. 11. An enhanced scatter-plot matrix represents 120 individual crystallizer configurations with the corresponding objective function OF_3 and the three geometrical design variables. These variables are illustrated by histograms in the main diagonal and all possible combinations of them are shown in the upper right part of the matrix. Fit-curves are also plotted for the scatter-plots. The corresponding linear regression values are provided in the lower left part of the matrix.

Detailed CFD-DEM models (CFD: Computational Fluid Dynamics; DEM: Discrete Element Method) can identify the CSD within the crystallizer along with the velocity profile. However, the associated computational effort is too high to simulate the entire process involving millions of crystals over a long process time. Thus, the advanced models can currently not fully replace the one-dimensional simulations. However, they can provide supplementary information.

An overview of more detailed models for describing the particle-laden flows has been given by [74] with particular emphasis on CFD-DEM simulations. In this model, all interactions that can occur between fluid and particles are taken into account [75]. Due to the strong increase in computer performance in recent decades, CFD-DEM become feasible for numerous applications [73,82–84].

To extend process understanding and to get more detailed insight a validated CFD-DEM model is applied [71]. In the DEM part, a softsphere approach is used with the correlations of [76] and [77], in which the DEM parameters are calibrated analogous to the procedure of [80] and [81]. The drag force that the fluid exerts on the particles is represented by the model of [79]. In principle, simple growth kinetics for the crystals can be specified in the DEM computation. Since the crystals would grow less than 1 µm in the short realizable time window of 60 s, growth is neglected in the presented simulations. Spherical particles are assumed in the CFD-DEM model since a separate study showed only negligible differences in the fluidization behavior compared to non-spherical crystals (designed as so-called particle bonds) in which considerably longer computation times were required. The CFD-DEM simulations are carried out with the open-source software CFDEMcoupling (coupling of OpenFOAM for CFD and LIGGGHTS for DEM) [78]. The fully automatic evolutionary geometry optimization is realized using our in-house software OPAL++ [70,72].

In order to perform an evolutionary optimization the computing time for a single individual should be kept relatively short, typically less than a day. Therefore, it was necessary to find a compromise between number of simulated particles and simulated physical time. The complete three-dimensional crystallization would require huge computational efforts in an optimization study; therefore, a CFD-DEM model based on a two-dimensional clip is developed and applied, as illustrated in Fig. 10. These CFD-DEM numerical simulations are fully automatically controlled by our in-house optimization library (OPAL++).

The computational geometry of the crystallization is parametrized by three design variables: the heights H_1 and H_2 and the radius R_2 (see Fig. 1). They were considered to be bound by the following intervals: $H_1 \in [0.5; 1.0\text{m}]$, $H_2 \in [0.2; 0.7\text{m}]$, $R_2 \in [0.015; 0.025\text{m}]$.

The radius R_1 was kept in this first optimization study constant at 0.0075 m and, thus, close to the values applied in the experimental study. Since the process performance is influenced by the variation of the operating conditions, the volumetric flowrate and the height of the product outlet nozzle were kept during the optimization constant and also close to the experimental situation ($\dot{V}_{in} = 9L/h$ and $H_{Prod} = 0.545m$).

As discussed above, important objectives of the crystallization process investigated are to:

- achieve high purity of the product
- improve productivity and yield (Eqs. (3) and (4))
- obtain a desired crystal size distribution (CSD).

In this analysis using a computationally expensive CFD-DEM

approach as the objective function, only the position of the product outlet is considered, where the samples were taken in a few selected time instants. The aim of the simulations performed was to optimize the CSD of the product in such a way that the largest possible number of crystals with a narrow size distribution can be withdrawn. Therefore, the number of crystals in the product with a large diameter ($L > 45\mu m$) should be maintained. Due to the classifying effect of the conical section, crystals with larger diameter (here $L > 266\mu m$) sink into the lower part of the crystallizer. For this reason they are not taken into account. The obtained particle distributions are combined in the following to be maximized objective function OF_3, where 6 different time snapshots are considered at the end of the simulated process time in every 4 s.

$$OF_3 = \frac{N_i(L > 45\mu\mathrm{m})}{N_{ges,i}} \rightarrow max, \quad with \;\; i = 1, \cdots, 6 \tag{19}$$

The computational mesh used in the simulations was created for all the considered cases fully automatically using ANSYS ICEMCFD (ANSYS Inc., Canonsburg, USA). 120 individual CFD-DEM numerical simulations are performed for all the considered cases. The optimization software environment based on by OPAL++ is basically designed for multi-objective optimization, but single-objective optimization (as in this case) can be realized as well. An important part of the optimization process is the definition of the evaluation chain for the individual. After a new generation has been created, the following procedure is carried out for all individuals which correspond to different crystallizer geometries:

1. Prepare a simulation setup and send the information to one of the computer nodes for evaluation.
2. Assemble an ICEMCFD-script with the corresponding design variables.
3. Produce a computational mesh in ICEMCFD and check its quality.
4. Implementation of the coupled CFD-DEM simulation.
5. Calculation of the objective function.

The objective function OF_3 and the three geometric design variables, H_1, H_2 and R_2, are depicted in condensed form in Fig. 11 using an enhanced scatter-plot matrix. 120 individual configurations are considered representing different geometries. In the main diagonal the frequency distributions for given parameters are represented by histograms. Individual scatter-plots of all the possible combinations are depicted in a matrix structure in the upper right part. They represent all the possible two-dimensional projections of the considered four-dimensional distribution. In Fig. 11 is shown furthermore a fit-curve for the scatter-plots to visualize a linear correlation between these variables. The corresponding linear regression value is also given in the corresponding part in the lower left part of the matrix. The font size of these values is scaled according to their values, where the strongest linear correlation is shown by the largest font-size.

The strongest linear correlation is obtained for the objective value and the height H_1. The second largest correlation can be found for the objective value and the radius R_2. This geometric optimization suggests relatively high H_1 values and possibly larger radius R_2 for the considered objective function. It can be observed that individuals with particularly good objective function are achieved when H_1 and R_2 have large values. The objective function considered so far (OF_3, Eq. (19)) seems to be rather independent of H_2. Based on the results described in Sections 5.2.3 and 6.2.1 there is another trend for the productivity considered as the objective function (Pr, Eq. (3)).

In summary, a fully automatic optimization has been realized with our in-house optimization software environment OPAL++ and coupled CFD-DEM simulations. In future investigations the optimized configurations will be investigated by experiments. Further numerical studies could incorporate the withdrawal strategy and further design variables, such as a modified height of the product outlet nozzle, modified volumetric flowrate, etc.

These first theoretical results of the detailed model and the tools developed are considered to be helpful for further optimizing the geometry and finding hydrodynamically critical positions of the conical shaped fluidized bed crystallizer and the process conditions.

8. Conclusions and outlook

We reported the current state of the art regarding continuous enantioselective crystallization of conglomerate forming systems applying preferential crystallization using two coupled conical shaped fluidized bed crystallizers. After reviewing the literature regarding crystallization-based enantioseparation it was successfully demonstrated that the process concept is applicable to efficiently resolve a racemic mixture. Exploiting a simple to implement periodic product withdrawal strategy the process provides for the resolution of the enantiomers of asparagine monohydrate an unprecedented high productivity reaching almost $Pr = 100g/L/h$. This exceeds significantly the current benchmark of $Pr_{max} = 20g/L/h$.

A spatially one-dimensional model described in this paper has been shown to possess good predictive capabilities and is seen as a strong tool for process design and optimization. It was applied to generate instructive predictions quantifying in particular a very promising periodic product withdrawal strategy. The effect of the geometry of the conically shaped crystallizers was evaluated as another very important degree of freedom. Regarding this aspect as an extension of the 1D model a detailed CFD-DEM based model was developed and first results are presented.

Finally, we would like to mention, that recently another successful application of the investigated process principle was achieved in resolving the two enantiomers of guaifenesin. Features of this more challenging system are the closer densities of solid and liquid phases and slower growth rates of needle-like crystals. In a future manuscript, we will compare these results with available results of batch-wise crystallization of guaifenesin reported in [34].

Declaration of Competing Interest

The authors declare that they have no known competing financial interests or personal relationships that could have appeared to influence the work reported in this paper.

Acknowledgments

The authors acknowledge the financial support of Deutsche Forschungsgemeinschaft (DFG) within the Priority Program “Dynamic Simulation of Interconnected Solids Processes (SPP 1679)”, the fruitful discussions with the members of the consortium and the excellent coordination work by the project manager Professor Stefan Heinrich. H.L. and A.S.-M. further thank the European Commission for support within the “CORE project” (CORE ITN project no. 722456). Furthermore, N.H. is grateful for the support by the “Research Center of Dynamic Systems (CDS)” of Otto von Guericke University Magdeburg.

Appendix A. Equations of the process model described in Section 5.1

The process model consists of population balances for the crystals in the crystallizer, component mass balances for the solutes in the liquid phase, and population balances for the crystals present in the mill. These balances hold for both enantiomers, here for $i = \text{D-Asn} \cdot H_20$, $j = \text{L-Asn} \cdot H_20$. Besides the coupling of the balances of the two crystallizers there is an additional coupling via the solubilty functions (Eq. (12)) exploited in the specific

Table A1
Additional parameters used in simulations with the model described in Section 5.1 and in this Appendix A.

Parameters related to the milling process (Eqs. (A.10) and (A.11))		
Critical length of crystals	L_c	390μm
Number of daughters from mill	p	10.8
kinetic parameter in breakage distribution function	q	0.2
kinetic parameter in breakage kernel	S_0	0.072
Parameters related to the heat transfer (Eqs. (A.13) and (A.14))		
heat transfer coefficient	α_{cool}	10 $Wm^{-2}K^{-1}$
proportional coefficient for the controller	k_p	95
integral coefficient for the controller	k_i	0.75

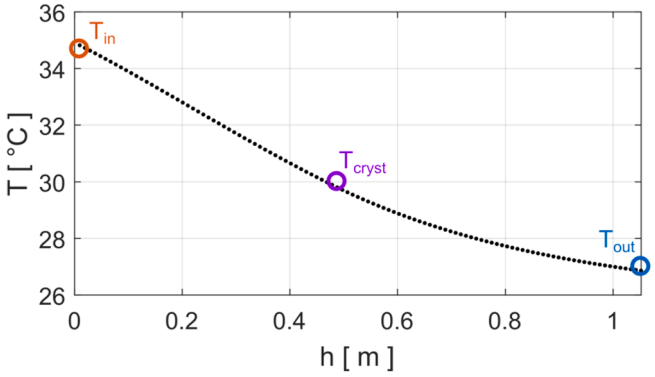

Fig. A1. Temperature distribution over crystallizer height. The symbols show measured values at the bottom (T_{in}), middle (T_{cryst}) and top (T_{out}) of the crystallizer. The line shows the simulated temperature distribution in the crystallizer with the estimated parameters given in Table A1.

supersaturations, $S_{i/j} = \frac{x_{i/j}}{x_{sat,i/j}}$. The model is an extended version of the model presented in [59]. For the sake of simplicity we present the models equation below without using component specific indices i and j.

Population balance for the particles in the crystallizer

The solid phase in the crystallizer is described by a number size density $n(h,L,t)$ A population balance gives

$$A(h)\left.\frac{\partial n}{\partial t}\right|_{h,L,t} = -\frac{\partial}{\partial h}\left(A(h)\cdot v_p(h,L,t)\cdot n(h,L,t)\right) - A(h)\cdot G\left(S_{i/j}\right)\left.\frac{\partial n}{\partial L}\right|_{h,L,t} + \dot{V}_M\cdot\left(n_M(L,t) - n(h,L,t)\right)\cdot\delta(h-h_M) \tag{A.1}$$

with boundary conditions

$$v_p(0,L,t)\cdot n(0,L,t) = 0 \tag{A.2}$$

$$\left.\frac{\partial n}{\partial h}\right|_{h,L,t} = 0 \tag{A.3}$$

$$G\left(S_{i/j}\right)\cdot n(h,0,t) = B(S_{i/j}) \tag{A.4}$$

and initial conditions

$$n(h,L,0) = n_0(h,L) \tag{A.5}$$

The first term on the right side of Eq. (A.1) describes the convective transport of particles with a velocity $v_p(h,L,t)$. $A(h)$ is the cross sectional area of the crystallizer. The second term stands for crystal growth with rate $G(S_{i/j})$. The third term describes the mass exchange with the mill. Hereby h_M denotes the position of the exchange; $\dot{V}_M$ is the volumetric flow to and from the mill and $n_M(L,t)$ is the number size density of the particles in the mill.

The equation and the parameters used to quantify the growth rates G were already introduced above. The rate law used has the following structure (Eq. (13)):

$$G(S_{i/j}) = k_g\cdot\left(S_{i/j}(T) - 1\right)^{n_g}\exp\left(-\frac{E_g}{R\cdot T}\right) \tag{A.6}$$

where $S_{i/j}(T)$ is the mentioned component (D or L) and temperature dependent supersaturation.

The nucleation rate B is incorporated via the boundary condition (Eq. (A.4)). Since the process is operated in a metastable zone the impact of this term is rather small. The nucleation rate was quantified using a similar expression as Eq. (A.6) with parameters estimated based on induction times observed in classical batch experiments.

Mass balance for the solute in the liquid phase

The mass balances for the enantiomers in the liquid phase of the crystallizer read

$$A(h)\frac{\partial}{\partial t}(\epsilon(h,t)c(h,t) = -\frac{\partial}{\partial h}\left(\dot{V}(h)c(h,t)\right) + \frac{\rho_{solid}}{\rho_{liquid}}\int_0^\infty A(h)\cdot G\frac{\partial n}{\partial L}\Big|_{h,L,t}\frac{\pi}{6}L^3dL + \frac{\rho_{solid}}{\rho_{liquid}}\int_0^\infty A(h)\cdot B\frac{\partial n}{\partial L}\Big|_{h,L,t}\frac{\pi}{6}L^3dL \tag{A.7}$$

To quantify the important effect of the inlet flow rate $\dot{V}_{in}$ we use also the following velocity:

$$u_{empty\ tube} = \frac{\dot{V}_{in}}{A(H_{prod})} \tag{A.8}$$

The volume fraction of the fluid $\epsilon(x,t)$ on the left hand-side considers the populations of both enantiomers and is given by

$$\epsilon(h,t) = 1 - \int_0^\infty n_i(h,L_i,t)\cdot\frac{\pi}{6}L_i^3dL_i - \int_0^\infty n_j(h,L,t)\cdot\frac{\pi}{6}L_j^3dL_j \tag{A.9}$$

Population balance for particles in the mill

Assuming perfect mixing in the disperser [62], the population balance equation for the number size density in the mill reads:

$$\frac{\partial n_M}{\partial t}\Big|_{L,t} = \int_L^\infty b(L,l)S_b(l)n_M(l,t)dl - S_b(L)n_M(l,t) + \frac{\dot{V}_M}{V_M}(n(L,t) - n_M(L,t)) \tag{A.10}$$

The following Hill-Ng breakage distribution function [66,67] is used to quantify $b(L,l)$

$$b(L,l) = K\frac{1}{l}\left(\frac{L}{l}\right)^{3(q-1)}\left(1-\left(\frac{L}{l}\right)^3\right)^{r-1}, r = q(p-1) \tag{A.11}$$

The parameter p is used for the number of daughter fragments after a breakage; q is a sharpness parameter [67]; K is a scaling constant. Exploiting the Heaviside function $H(L-L_c)$, the following equation is used for the breakage kernel $S_b(L)$:

$$S_b(L) = S_0H(L-L_c) \tag{A.12}$$

The critical length of the particle L_c is chosen according to experimental observations.

In summary, the model of the mill contains the kinetic parameters p, q and S_0, which are listed together with L_c in Table A1. The procedure applied for parameter estimation is described in [59].

Energy balance of crystallizer

In order to be able to incorporate into the solution temperature changes during the process the following energy balance equation is solved:

$$\begin{aligned}\left(A\epsilon(\rho_{liquid}\cdot c_{p\,liquid}) + A(1-\epsilon)\rho_{solid}\cdot c_{p\,solid}\right)\frac{\partial T}{\partial t} = &-\left(\dot{V}\cdot\rho_{liquid}\cdot c_{p\,liquid} - A\cdot\rho_{solid}\cdot c_{p\,solid}\left(\int_0^\infty v_{p,i}n_i\frac{\pi}{6}L_i^3L_i + \int_0^\infty v_{p,j}n_j\frac{\pi}{6}L_j^3L_j\right)\right)\frac{\partial T}{\partial h}\\ &-\Delta H_{cryst}\cdot\rho_{solid}\mathrm{A}\left(\int_0^\infty G\frac{\partial n_i}{\partial L_i}\frac{\pi}{6}L_i^3dL_i + \int_0^\infty G\frac{\partial n_j}{\partial L_j}\frac{\pi}{6}L_j^3dL_j\right)\\ &+\dot{V}_M\left(\left(\rho_{liquid}\cdot c_{p\,liquid}\right) + \rho_{solid}\cdot c_{p\,solid}\int_0^\infty n_M\frac{\pi}{6}L^3dL\right)(T_M - T)\delta(h-h_M) + \alpha_{cool}\pi d(h)(T_{cool}-T)\end{aligned} \tag{A.13}$$

- The first line on the right-hand side describes temperature changes due to transport of liquid and particles along the height coordinate.
- The second line on the right-hand side describes temperature changes due to heat of crystallization.
- The third term quantifies the heat exchange between mill and crystallizer.
- The last term describes heat exchange between crystallizer and a coolant of specified temperature T_{cool} using a heat transfer coefficientα_{cool}. In the experiments a PI feedback controller was used to keep the temperature in the middle of the crystallizer at a desired value, T_{cryst}.

$$T_{cool} = k_p\left(T_{cryst} - T_i\right) + k_i\int_0^t (T_{cryst} - T_i)dt \tag{A.14}$$

Thus additional model parameters are the proportional and integral coefficients of the temperature controller applied, namely k_p and k_i. These parameters were adjusted to match experimentally observed temperature. An example for a comparison between simulated and experimentally determined axial temperature profiles is shown in Fig. A1. The additionally determined parameters used in the simulations are summarized in Table A1.

The numerical solution of the set of model equations is similar to the approaches in [64,65]. Using the method of lines, the model equations are discretized on a grid with 110 equidistant grid points on the h coordinate and 100 equidistant grid points on the L coordinate. The periodical steady state solutions are obtained by a time integration of the resulting ODE system using the initial value problem solver ODE23 implemented in MATLAB [69]. The integration is stopped when the ratio between the sum of all mass flows across the system boundary and the mass flow into the system, falls below a threshold of 10^{-5}. For test parameter optimization, the CMAES algorithm is used [68].

Appendix B. Variations of crystallizer geometry

Two pairs of crystallizers were experimentally studied (Section 6.3) and simulated via the process model (Section 5.2.4). The first pair of crystallizers were manufactured according to the “Reference geometry (Cref-D, Cref-L), and were utilized in previous experimental studies [47,50]. The

Table B1
Crystallizer dimensions measured (notation as in Fig. 1), the resulting cone opening angle, α, and the total volume, V_{tot}, of the two crystallizers with "Reference geometry" (Cref-D, Cref-L) and of the two manufactured new crystallizers with "Adjusted geometry" (Cadj-D, Cadj-L).

Cryst.	Seeds	R_1 [m]	R_2 [m]	H_1 [m]	H_2 [m]	H_{prod} [m]	α [°]	V_{total} [L]
Cref-D	D-Asn·H_2O	0.005636	0.01305	0.456	0.598	0.319	1.87	0.478
Cref-L	L-Asn·H_2O	0.006291	0.01380	0.490	0.562	0.335	1.76	0.511
Cadj-D	D-Asn·H_2O	0.009788	0.01882	0.505	0.259	0.345	2.05	0.665
Cadj-L	L-Asn·H_2O	0.01027	0.01890	0.510	0.247	0.356	1.94	0.665

second pair are newly manufactured according to the "Adjusted geometry" (Cadj-D, Cadj-L), which was suggested in a previous simulation study [59]. The measured dimensions of the four crystallizers are summarized in Table B1.

Appendix C. Analytical methods applied to characterize the crystalline product

Identical experimental procedures were applied as described in [50]. The withdrawn, filtered, washed and dried product crystals were analyzed via high performance liquid chromatography (HPLC) after dissolution of the solid phase, X-ray powder diffraction (XRPD) and sieve analysis. Specifications of the methods applied are summarized in Table C1.

Table C1
Specifications of the applied analysis methods.

Method	Specification
HPLC	Crownpak CR(+) (4x150 mm, particle size 5 µm) column (Chiral Technologies, France) with Dionex Ultimate 3000 system (Thermo Scientific, Country)). Perchloric acid/ water (pH = 1) as the eluent. The flow rate, UV wave length, column temperature and injection volume were 0.4 ml/min, 200 nm, 5 °C and 1 µl, respectively.
XRPD	X'Pert Pro diffractometer (PANalytical GmbH, Germany), 2-theta range of 5-40°, step size 0.017°, step time 50 s
Sieve analysis	AS 200 digit, amplitude 1.8 mm, sieving time 20 min, sieve mesh widths: 0, 90, 125, 180, 212, 250, 300, 355, 400, 500, 630, 710, 800 µm (Retsch, Germany)

References

[1] E.L. Eliel, S.H. Wilen, M.P. Doyle, Basic organic stereochemistry, Org. Proc. Res. Dev. 6 (2002) 201–204, https://doi.org/10.1021/op010106u.
[2] U. Meierhenrich, Amino Acids and the Asymmetry of Life, Springer, Berlin, 2008.
[3] P. Herdewijn, M.V. Kisakürek, Origin of Life – Chemical Approach, Helvetica Chimica Acta, Zürich, 2008.
[4] R.A. Sheldon, Chirotechnology: Industrial Synthesis of Optically Active Compounds, Marcel Dekker, New York, 1993.
[5] A.M. Rouhi, Fine chemicals companies are jockeying for position to deliver the increasingly complicated chiral small molecules of the future, Chem. Eng. News 81 (2003) 45–55.
[6] B.A. Asteleford, L.O. Weigel in Chirality in industry II. Developments in the manufacture and applications of optically active compounds, (Eds.: A. Collins, G. Sheldrake, J. Crosby), John Wiley & Sons, Chichester, 1997, pp. 119–156.
[7] J. Crosby, Introduction, in: A. Collins, G. Sheldrake, J. Crosby (Eds.), Chirality in industry II. Developments in the commercial manufacture and applications of optically active compounds, Chichester, John Wiley & Sons, pp. 1–10.
[8] H. Lorenz, A. Seidel-Morgenstern, Processes to separate enantiomers, Angew. Chem. Int. Ed. 53 (5) (2014) 1218–1250, https://doi.org/10.1002/anie.201302823.
[9] R. Noyori, Asymmetric Catalysis in Organic Synthesis, Wiley, New York, 1994.
[10] A. Berkessel, H. Grcger, Asymmetric Organocatalysis: From Biomimetic Concepts to Applications in Asymmetric Synthesis, Wiley, New York, 2005.
[11] H.U. Blaser, H.-J. Federsel, Asymmetric Synthesis on Industrial Scale, second ed., Wiley-VCH, Weinheim, 2010.
[12] E. Francotte, Chiral stationary phases for preparative enantioselective chromatography, in: G.B. Cox (Ed.), Preparative Enantioselective Chromatography, Blackwell Publishing Ltd, Oxford, UK, 2005, pp. 48–77.
[13] A. Rajendran, G. Paredes, M. Mazzotti, Simulated moving bed chromatography for the separation of enantiomers, J. Chromatogr. A 1216 (4) (2009) 709–738, https://doi.org/10.1016/j.chroma.2008.10.075.
[14] N.S. Tavare, Industrial Crystallization: Process Simulation, Analysis and Design, Plenum PressNew York and London, 1995.
[15] J.W. Mullin, Crystallization, fourth ed., Butterworth-Heinemann, Oxford, Boston, 2001.
[16] A. Mersmann, Crystallization Technology Handbook, Marcel Dekker Inc., Basel, 2001.
[17] A. Cybulski, M.M. Sharma, R.A. Sheldon, J.A. Moulijn, Fine Chemicals Manufacture – Technology and Engineering, Elsevier, Amsterdam, 2001.
[18] W. Beckmann, Crystallization: Basic Concepts and Industrial Applications, Wiley-VCH, Weinheim, 2013.
[19] H. Lorenz, Solubility and Solution Equilibria in Crystallization, in: W. Beckmann (Ed.), Crystallization: Basic Concepts and Industrial Applications, Wiley-VCH Verlag GmbH & Co. KGaA, Weinheim, Germany, 2013, pp. 35–74.
[20] N. Yazdanpanah, Z.K. Nagy, The Handbook of Continuous Crystallization, Royal Society of Chemistry, Cambridge, 2020.
[21] M.o. Jiang, R.D. Braatz, Designs of continuous-flow pharmaceutical crystallizers: developments and practice, CrystEngComm 21 (23) (2019) 3534–3551, https://doi.org/10.1039/C8CE00042E.
[22] H. Lorenz, E. Temmel, A. Seidel-Morgenstern, Continuous enantioselective crystallization of chiral compounds. Chapter 12, in: N. Yazdanpanah, Z.K. Nagy (Eds.), The Handbook of Continuous Crystallization, Royal Society of Chemistry, Cambridge, 2020, pp. 422–468.
[23] A. Myerson, Handbook of Industrial Crystallization, Butterworth-Heinemann, 2002.
[24] R.J.P. Eder, S. Radl, E. Schmitt, S. Innerhofer, M. Maier, H. Gruber-Woelfler, J. G. Khinast, Continuously seeded, continuously operated tubular crystallizer for the production of active pharmaceutical ingredients, Cryst. Growth Des. 10 (5) (2010) 2247–2257, https://doi.org/10.1021/cg9015788.
[25] X. Ni, Continuous crystallization with oscillatory baffled crystallizer technology, in: N. Yazdanpanah, Z.K. Nagy (Eds.), The Handbook of Continuous Crystallization, Royal Society of Chemistry, Cambridge, 2020, pp. 102–171.
[26] L. Hohmann, T. Greinert, O. Mierka, S. Turek, G. Schembecker, E. Bayraktar, K. Wohlgemuth, N. Kockmann, Analysis of crystal size dispersion effects in a continuous coiled tubular crystallizer: experiments and modeling, Cryst. Growth Des. 18 (3) (2018) 1459–1473, https://doi.org/10.1021/acs.cgd.7b01383.s002.
[27] M. Su, Y. Gao, Air–liquid segmented continuous crystallization process optimization of the flow field, growth rate, and size distribution of crystals, Ind. Eng. Chem. Res. 57 (10) (2018) 3781–3791, https://doi.org/10.1021/acs.iecr.7b05236.
[28] J. Jacques, A. Collet, S.H. Wilen, Enantiomers, Racemates, and Resolutions, Krieger, Malabar, 1994.
[29] A. Collet, Separation and purification of enantiomers by crystallization methods, Enantiomer 4 (1999) 157–172.
[30] G. Coquerel, Preferential crystallization, Top. Curr. Chem. 269 (2007), in: K. Sakai, H. Hirayama, R. Tamura (Eds.), Novel Optical Resolution Technologies, Springer-Verlag, Berlin-Heidelberg, 2006, pp. 1–51.
[31] M.P. Elsner, G. Ziomek, A. Seidel-Morgenstern, Simultaneous preferential crystallization in a coupled batch operation mode. Part II: Experimental study and model refinement, Chem. Eng. Sci. 66 (2011) 1269–1284, https://doi.org/10.1016/j.ces.2010.12.035.
[32] M.J. Eicke, Process Strategies for Batch Preferential Crystallization, Ph.D. thesis, Otto von Guericke University Magdeburg, Shaker, Aachen, 2016.
[33] G. Levilain, M.J. Eicke, A. Seidel-Morgenstern, Efficient resolution of enantiomers by coupling preferential crystallization and dissolution. Part 1: Experimental proof of principle, Cryst. Growth Des. 12 (2012) 5396–5401, https://doi.org/10.1021/cg3009943.
[34] E. Temmel, M.J. Eicke, F. Cascella, A. Seidel-Morgenstern, H. Lorenz, Resolution of racemic guaifenesin applying a coupled preferential crystallization-selective dissolution process: rational process development, Cryst. Growth Des. 19 (2019) 3148–3157, https://doi.org/10.1021/acs.cgd.8b01660.

[35] H.-H. Tung, E.L. Paul, M. Midler, J.A. McCauley, Crystallization of Organic Compounds: An Industrial Perspective, John Wiley & Sons, Hoboken, 2009.
[36] Y. Ma, S. Wu, E.G.J. Macaringue, T. Zhang, J. Gong, J. Wang, Recent progress in continuous crystallization of pharmaceutical products: precise preparation and control, Org. Process Res. Dev. 24 (2020) 1785–1801, https://doi.org/10.1021/acs.oprd.9b00362.
[37] D. Zhang, S. Xu, S. Du, J. Wang, J. Gong, Progress of pharmaceutical continuous crystallization, Engineering 3 (2017) 354–364, https://doi.org/10.1016/J.ENG.2017.03.023.
[38] C. Darmali, S. Mansouri, N. Yazdanpanah, M.W. Woo, Mechanisms and Control of Impurities in Continuous Crystallization: A Review, Ind. Eng. Chem. Res. 58 (2019) 1463–1479, https://doi.org/10.1021/acs.iecr.8b04560.
[39] L. Synoradzki, H. Hajmowicz, J. Wisialski, A. Mizerski, T. Rowicki, Calcium pantothenate. Part 3. Process for the biologically active enantiomer of the same via selective crystallization and racemization, Org. Process Res. Dev. 12 (2008) 1238–1244, https://doi.org/10.1021/op800189g.
[40] M. Leeman, F. Querniard, T.R. Vries, B. Kaptein, R.M. Kellogg, The resolution of 2-hydroxy-5,5-dimethyl-4-phenyl-1,3,2-dioxaphosphorinan 2-oxide (phencyphos) by preferential crystallization, Org. Process Res. Dev. 13 (2009) 1379–1381, https://doi.org/10.1021/op900171k.
[41] T. Kollges, T. Vetter, Design and performance assessment of continuous crystallization processes resolving racemic conglomerates, Cryst. Growth Des. 18 (2018) 1686–1696, https://doi.org/10.1021/acs.cgd.7b01618.
[42] C. Maharaj, J. Chivavava, A. Lewis, Treatment of a highly-concentrated sulphate-rich synthetic wastewater using calcium hydroxide in a fluidised bed crystallizer, J. Environ. Manage. 207 (2018) 378–386, https://doi.org/10.1016/j.jenvman.2017.09.061.
[43] Y.J. Shih, R.R.M. Abarca, M.D.G. de Luna, Y.H. Huang, M.C. Lu, Recovery of phosphorus from synthetic wastewaters by struvite crystallization in a fluidized-bed reactor: effects of pH, phosphate concentration and coexisting ions, Chemosphere 173 (2017) 466–473, https://doi.org/10.1016/j.chemosphere.2017.01.088.
[44] X. Vu, J.-Y. Lin, Y.-J. Shih, Y.-H. Huang, Reclaiming boron as calcium perborate pellets from synthetic wastewater by integrating chemical oxo-precipitation within a fluidized-bed crystallizer, ACS Sustain. Chem. Eng. 6 (2018) 4784–4792, https://doi.org/10.1021/acssuschemeng.7b03951.
[45] D. Guillard, A.E. Lewis, Nickel carbonate precipitation in a fluidized-bed reactor, Ind. Eng. Chem. Res. 40 (2001) 5564–5569, https://doi.org/10.1021/ie010312q.
[46] R. Aldaco, A. Garea, A. Irabien, Fluoride recovery in a fluidized bed: crystallization of calcium fluoride on silica sand, Ind. Eng. Chem. Res. 45 (2006) 796–802, https://doi.org/10.1021/ie050950z.
[47] D. Binev, A. Seidel-Morgenstern, H. Lorenz, Continuous Separation of isomers in fluidized bed crystallizers, Cryst. Growth Des. 16 (2016) 1409–1419, https://doi.org/10.1021/acs.cgd.5b01513.
[48] D. Binev, A. Seidel-Morgenstern, H. Lorenz, Study of crystal size distributions in a fluidized bed crystallizer, Chem. Eng. Sci. 133 (2015) 116–124, https://doi.org/10.1016/j.ces.2014.12.041.
[49] D. Binev, Continuous fluidized bed crystallization, PhD thesis, Otto von Guericke University Magdeburg, 2014.
[50] E. Temmel, J. Gänsch, H. Lorenz, A. Seidel-Morgenstern, Systematic investigations on continuous fluidized bed crystallization for chiral separation, Crystals 10 (2020) 394–409, https://doi.org/10.3390/cryst10050394.
[51] R. Kacker, S. Maaß, J. Emmerich, H. Kramer, Application of inline imaging for monitoring crystallization process in a continuous oscillatory baffled crystallizer, AICHE J. 64 (2018) 2450–2461, https://doi.org/10.1002/aic.16145.
[52] H.M. Huffman, H. Borsook, Thermal data. I. The heat capacities, entropies and free energies of seven organic compounds containing nitrogen, J. Am. Chem. Soc. 54 (1932) 4297–4301.
[53] K. Petruševska-Seebach, Overcoming Yield Limitations When Resolving Racemates by Combination of Crystallization and/or Chromatography with Racemization, PhD thesis, Otto von Guericke University Magdeburg, docupoint Wissenschaft, Barleben, 2012.
[54] E. Temmel, H. Eisenschmidt, H. Lorenz, K. Sundmacher, A. Seidel-Morgenstern, A short-cut method for the quantification of crystallization kinetics, Cryst. Growth Des. 16 (2016) 6743–6755, https://doi.org/10.1021/acs.cgd.6b00787.
[55] E. Temmel, J. Gänsch, H. Lorenz, A. Seidel-Morgenstern, Measurement and evaluation of the crystallization kinetics of L-asparagine monohydrate in the ternary L-/D-asparagine/water system, Cryst. Growth Des. 18 (2018) 7504–7517, https://doi.org/10.1021/acs.cgd.8b01322.
[56] M. Mazzotti, M. Iggland, A population balance model for chiral resolution via viedma ripening, Cryst. Growth Des. 11 (2011) 4611–4622, https://doi.org/10.1021/cg2008599.
[57] M. Mangold, L. Feng, D. Khlopov, S. Palis, P. Benner, D. Binev, A. Seidel-Morgenstern, Nonlinear model reduction of a continuous fluidized bed crystallizer, J. Comput. Appl. Math. 289 (2015) 253–266, https://doi.org/10.1016/j.cam.2015.01.028.
[58] T. Vetter, C. Burcham, M. Doherty, Separation of conglomerate forming enantiomers using a novel continuous preferential crystallization process, AIChE J 61 (2015) 2810–2823, https://doi.org/10.1002/aic.14934.
[59] M. Mangold, D. Khlopov, E. Temmel, H. Lorenz, A. Seidel-Morgenstern, Modelling geometrical and fluid-dynamic aspects of a continuous fluidized bed crystallizer for separation of enantiomers, Chem. Eng. Sci. 160 (2017) 281–290, https://doi.org/10.1016/j.ces.2016.11.042.
[60] M. Lorenzo, C. Silvestre, Non-isothermal crystallization of polymers, Prog. Polym. Sci. 24 (1999) 917–950, https://doi.org/10.1016/S0079-6700(99)00019-2.
[61] J. Richardson, W. Zaki, The sedimentation of a suspension of uniform spheres under conditions of viscous flow, Chem. Eng. Sci. 3 (1954) 65–73, https://doi.org/10.1016/0009-2509(54)85015-9.
[62] V. Spillar, D. Dolejs, Calculation of time-dependent nucleation and growth rates from quantitative textural data: inversion of crystal size distribution, J. Petrol. 54 (2013) 913–931, https://doi.org/10.1093/petrology/egs091.
[63] G. Reynolds, Modelling of pharmaceutical granule size reduction in a conical screen mill, Chem. Eng. J. 164 (2010) 383–392, https://doi.org/10.1016/j.cej.2010.03.041.
[64] T. Köllges, T. Vetter, Polymorph selection and process intensification in a continuous crystallization-milling process: a case study on L-glutamic acid crystallized from water, Org. Process Res. Dev. 23 (3) (2019) 361–374, https://doi.org/10.1021/acs.oprd.8b00420.
[65] Z. Ulbert, B.G. Lakatos, Dynamic simulation of crystallization processes: adaptive finite element collocation method, AIChE J. 53 (2007) 3089–3107, https://doi.org/10.1002/aic.11303.
[66] P. Hill, K. Ng, Statistics of multiple particle breakage, AIChE J. 42 (1996) 1600–1611, https://doi.org/10.1002/aic.690420611.
[67] R. Diemer, D. Spahr, J. Olson, R. Magan, Interpretation of size reduction data via moment models, Powder Technol. 156 (2005) 83–94, https://doi.org/10.1016/j.powtec.2005.04.015.
[68] N. Hansen, The CMA evolution strategy: a comparing review, in: J.A. Lozano, P. Larrañaga, I. Inza, E. Bengoetxea (Eds.), Towards a new Evolutionary Computation. Advances on Estimation of Distribution Algorithms, Springer, 2006, pp. 75–102.
[69] MATLAB, The MathWorks Inc. Natick, Massachusetts, United States; [9.1.0.960167], Version 2016b.
[70] M. Mansour, K. Zähringer, K.D.P. Nigam, D. Thévenin, G. Janiga, Multi-objective optimization of liquid-liquid mixing in helical pipes using Genetic Algorithms coupled with Computational Fluid Dynamics, Chem. Eng. J. 391 (2020), 123570, https://doi.org/10.1016/j.cej.2019.123570.
[71] K. Kerst, C. Roloff, L. Medeiros de Souza, A. Bartz, A. Seidel-Morgenstern, D. Thévenin, G. Janiga, CFD-DEM simulations of a fluidized bed crystallizer, Chem. Eng. Sci. 165 (2017) 1–13, https://doi.org/10.1016/j.ces.2017.01.068.
[72] L. Daróczy, G. Janiga, D. Thévenin, Systematic analysis of the heat exchanger arrangement problem using multi-objective genetic optimization, Energy 65 (2014) 364–373, https://doi.org/10.1016/j.energy.2013.11.035.
[73] B. Ashraf Ali, M. Börner, M. Peglow, G. Janiga, A. Seidel-Morgenstern, D. Thévenin, Coupled computational fluid dynamics – discrete element method simulations of a pilot-scale batch crystallizer, Cryst. Growth Des. 15 (2015) 145–155, https://doi.org/10.1021/cg501092k.
[74] C.K. Harris, D. Roekaerts, F.J.J. Rosendal, F.G.J. Buitendijk, P. Daskopoulos, A.J. N. Vreenegoor, H. Wang, Computational fluid dynamics for chemical reactor engineering, Chem. Eng. Sci. 51 (1996) 1569–1594, https://doi.org/10.1016/0009-2509(96)00021-8.
[75] C.T. Crowe, Multiphase Flow Handbook, Taylor and Francis, Boca Raton USA, 2005.
[76] H. Hertz, Über die Berührung fester elastischer Körper, J. Reine Angew. Math. 92 (1882) 156–171.
[77] R.D. Mindlin, Compliance of elastic bodies in contact, J. Appl. Mech. 16 (1949) 259–268.
[78] C. Goniva, C. Kloss, N.G. Deen, J.A.M. Kuipers, S. Pirkers, Influence of rolling friction on single spout fluidized bed simulation, Particuology 10 (2012) 582–591, https://doi.org/10.1016/j.partic.2012.05.002.
[79] R. Di Felice, The voidage function for fluid-particle interaction systems, Int. J. Multiph. Flow 20 (1) (1993) 153–159, https://doi.org/10.1016/0301-9322(94)90011-6.
[80] H. Otto, K. Kerst, C. Roloff, G. Janiga, A. Katterfeld, CFD–DEM simulation and experimental investigation of the flow behavior of lunar regolith JSC-1A, Particuology 40 (2018) 34–43, https://doi.org/10.1016/j.partic.2017.12.003.
[81] T. Roessler, A. Katterfeld, Scaling of the angle of repose test and its influence on the calibration of DEM parameters using upscaled particles, Powder Technol. 330 (2018) 58–66, https://doi.org/10.1016/j.powtec.2018.01.044.
[82] M. Maestri, G. Salierno, S. Piovano, M. Cassanello, M.A. Cardona, D. Hojman, H. Somacal, CFD-DEM modeling of solid motion in a water-calcium alginate fluidized column and its comparison with results from radioactive particle tracking, Chem. Eng. J. 377 (2019), 120339, https://doi.org/10.1016/j.cej.2018.11.037.
[83] M. Trofa, G. D'Avino, L. Sicignano, G. Tomaiuolo, F. Greco, P.L. Maffettone, S. Guido, S, CFD-DEM simulations of particulate fouling in microchannels, Chem. Eng. J. 358 (2019) 91–100, https://doi.org/10.1016/j.cej.2018.09.207.
[84] C. Moliner, F. Marchelli, N. Spanachi, A. Martinez-Felipe, B. Bosio, E. Arato, CFD simulation of a spouted bed: comparison between the Discrete Element Method (DEM) and the Two Fluid Model (TFM), Chem. Eng. J. 377 (2019), 120466, https://doi.org/10.1016/j.cej.2018.11.164.